Detrital orthopyroxene as a tracer of geodynamic setting: a Raman and SEM-EDS provenance study

Short title: Detrital orthopyroxene as provenance tracer

Laura Borromeo[1*], Sergio Andò[1], Danilo Bersani[2], Eduardo Garzanti[1], Paolo Gentile[3], Luciana Mantovani[2], Mario Tribaudino[4]

[*] Correspondence to: University of Milano-Bicocca, Piazza della Scienza, 4, 20126, Milano (Italy)
E-mail: laura.borromeo@unimib.it

[1] Laboratory for Provenance Studies, Department of Earth and Environmental Sciences, University of Milano-Bicocca, 20126, Milano (Italy)

[2] Department of Mathematical, Physical and Computer Sciences, University of Parma, Parma, 43124, (Italy)

[3] Platform of Microscopy, Department of Earth and Environmental Sciences, University of Milano-Bicocca, 20126, Milano (Italy)

[4] Department of Earth Sciences, University of Torino, 10124, Torino, (Italy)

ABSTRACT

Raman spectroscopy is a powerful tool that for its efficiency is being used more and more frequently in high-resolution provenance analysis. In this study, dedicated to Ca-poor orthorhombic pyroxene, we focused on 15 samples of modern sands representing a full range of rock units exposed at different structural levels of continental, arc, or oceanic lithosphere and generated in diverse geodynamic settings. By coupling optical observations, SEM-EDS minerochemical and Raman spectroscopy analyses on the same grains we show how orthopyroxene from mantle, deep crustal, and volcanic rocks ranging in composition from andesite to dacite and felsic differentiates can be robustly distinguished. The Mg# [Mg/(Mg+Fe)] content of orthopyroxene grains can be accurately estimated by recording the characteristic position of their six main characteristic peaks (ν_1 to ν_6, vibrational modes) even during routine point-counting under the Raman spectroscope. Most useful at this regard is the position of the strong and narrow ν_3 peak (~655 cm^{-1}) that also allows to estimate Ca content if compared with the position of other peaks (especially ν_1, ~330 cm^{-1}). High-Mg orthopyroxene is exclusively derived from mantle rocks, whereas metagabbros of the lower continental crust and gabbroic rocks of the arc crust could be distinguished by their lower Ca.

The lowest Mg# was recorded in detrital orthopyroxene derived from the silicic Amiata Volcano in central Italy, whereas trachytes in rift-related settings did not show peculiar characteristics apart from their slightly higher Ca content.

Key Words: Provenance analysis; Enstatite; Hypersthene; Raman Spectroscopy; SEM-EDS chemical analyses; Volcanic orthopyroxene.

1. Introduction

In the last years, multi-method approaches to provenance analysis have provided a bounty of information on sedimentary systems, improving our understanding of physical and chemical processes that control the modification of provenance signals during sediment transfer from source to sink (Garzanti, 2016; Basu, 2017; Caracciolo, 2020). Techniques focusing on specific detrital minerals or mineral groups have resulted to be particularly fruitful and exploited (Mange and Morton, 2007; von Eynatten and Dunkl, 2012; Guo et al., 2020). Zircon played the lion's share (Gehrels, 2011) and attentions were primarily dedicated to the composition of durable species, including rutile (Meinhold, 2010), tourmaline (Guo et al., 2021), apatite (O'Sullivan et al., 2020), garnet (Suggate and Hall, 2014), or Cr-spinel (Hu et al., 2014). Less specific attention was dedicated to less durable ferromagnesian minerals (e.g., Lee et al., 2003; Andò and Garzanti, 2014; Liang et al., 2019). This is largely because diagenized ancient sandstones generally contain only those species that better resist intrastratal dissolution, whereas amphiboles and especially pyroxenes and olivine are seldom preserved in ancient sandstones (Morton and Hallsworth, 2007; Garzanti et al., 2018). The durability of detrital minerals, however, may also represent a disadvantage, because grains can be easily recycled from one sedimentary cycle to the next thus loosing all information on the routing of detritus (Andersen et al., 2016; Pastore et al., 2021). Conversely, where preserved, less durable ferromagnesian minerals such as pyroxene are likely to be first cycle and thus able to deliver information pointing directly to their igneous or metamorphic source-rocks (Cawood, 1983; Caracciolo et al., 2016).

This modern-sand provenance study contributes to fill the existing knowledge gap concerning the distribution of pyroxene species in sediments, with the main aim to assess the relationship between pyroxene composition and the lithology of source rocks generated in diverse geodynamic settings. Here we shall focus on the simpler Ca-poor orthorhombic orthopyroxenes (OPX), whereas the much more complex relation between clinopyroxene composition and Raman spectra will be tackled in separate articles.

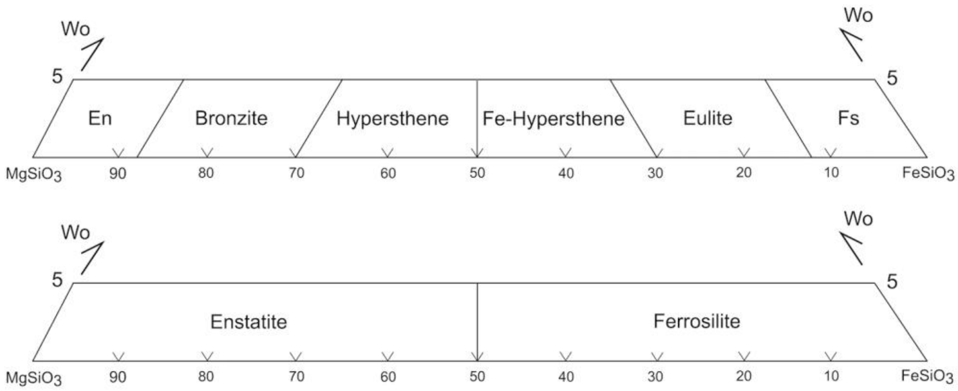

Figure 1. Comparison between traditional (upper panel; Poldervaart and Hess, 1947) and IMA (lower panel; Morimoto et al., 1988) orthopyroxene classification schemes. En: enstatite; Fs: ferrosilite; Wo: wollastonite.

In the traditional classification scheme (Poldervaart, 1947), orthopyroxenes were classified based on their Mg/(Mg+Fe) atomic ratio (Mg#), as enstatite, bronzite, hypersthene, Fe-hypersthene, eulite, or ferrosilite (Fig. 1). The current nomenclature of the International Mineralogical Association (IMA), instead, more simply distinguishes between enstatite *s.l.* (Mg# > 0.5) and ferrosilite *s.l.* (Mg# < 0.5) (Morimoto et al., 1988). Magnesium-rich orthopyroxene (enstatite *s.s.*) characterizes ultramafic rocks (e.g., harzburgite, orthopyroxenite, kimberlite; Eggler, 1986; Rezvukhin et al., 2019), and occurs in magnesian skarn and achondrite (Skridlaitė et al., 2019; Lorenz et al., 2020). Instead, iron-bearing orthopyroxene (hypersthene *s.l.*), characterizes anorthosite (Morse, 1975), tonalite, monzonite (Leslie et al., 2003), andesite (Francalanci et al., 2005), and more felsic lavas and pyroclastic rocks (Aoki, et al., 1989), and occurs in granulite (Jan and Howie, 1980) or meteoritic chondrite (Kubovics et al., 2004). Iron-rich orthopyroxene (Mg# < 0.3) is rare in rocks, and pure ferrosilite very rare (Bowen, 1935, Lindsley, 1965) with a few crystals identified in meteorites (Gismelseed et al., 2005).

In sedimentary petrography, it is common use to distinguish only two categories of orthopyroxene: the nearly colourless, optically positive magnesium-rich orthopyroxene (enstatite *s.s.*; Poldervaart, 1947) from strongly pleochroic, optically negative iron-bearing orthopyroxene (hypersthene *s.l.*, including bronzite, hypersthene, and Fe-hypersthene; Tröeger, 1979; Mange and Maurer, 1992). The correct determination of pyroxene species by both optical and electron-beam methods may however represent a challenge (Dunkl et al., 2020 p.18). A full objective discrimination among orthopyroxenes of different chemical composition is generally impossible under the microscope, and small grains lacking colour or cleavage, or showing high roundness, alteration, or unusual birefringence and interference figures may even be misidentified as epidote or olivine.

These difficulties can be overcome by obtaining decisive information with Raman spectroscopy, a simple-to-perform technique that, in a few seconds and with no additional sample preparation, allows us to achieve a robust mineralogical characterization (e.g., Griffith, 1969; Hope et al. 2001; Bersani et al., 2009). Grains can be successfully identified even down to the size of a few microns (Delmonte et al. 2017; Borromeo et al. 2018), also obtaining semi-quantitative crystallographic and chemical information. This non-destructive technique is excellently suited to investigate minerals and mineral inclusions (Raman, 1928; Griffith, 1969; Frezzotti et al. 2012), the specific lattice features of which are readily revealed by their direct link with Raman peak positions. In the case of vicariance, the different characteristics of the replacing ions produces variations in the strength and geometry of chemical bonds, and such differences in mineral structure are mirrored in Raman spectra (Kuebler et al. 2006; Borromeo et al., 2017; Bersani et al. 2018). Preliminary investigations on synthetic and selected natural pyroxenes have shown that chemical and structural changes can be modelled by Raman spectroscopy in both orthorhombic and monoclinic pyroxenes (e.g., Tribaudino et al., 2019; Stangarone et al., 2021).

In a multi-technique approach we combine optical, Raman spectroscopy, and SEM-EDS minerochemical analyses conducted on the same grains not only to increase the robustness of precise orthopyroxene identification but, especially, to establish the relationships among optical properties (e.g., pleochroism and birefringence), chemical composition (e.g., relative amounts of Mg, Fe, and Ca), and Raman signature (i.e., position of principal and secondary peaks) of detrital orthopyroxene. Specifically, we aim to demonstrate how Raman spectroscopy can be routinely used in high-resolution heavy-mineral analysis to efficiently assess the chemistry of pyroxene grains and thus obtain reliable information on the lithology of source rocks (e.g., peridotite, gabbro, andesite, dacite) and precious hints on the most plausible lithogenetic process (i.e., intrusive, effusive, or metamorphic) and geodynamic environment in which it took place (e.g., ophiolite obduction, continental rift, oceanic or continental subduction).

2. Orthopyroxene & Raman: state of the art

Pyroxenes are chain silicates of general formula $M2M1Si_2O_6$. In natural pyroxenes, the M2 and M1 sites are filled by Mg, Fe^{2+}, Ca, Li, Mn, or Na and by Mg, Fe^{2+}, Fe^{3+}, Al, Cr, or Ti^{4+}, Ti^{3+}, Mn (and others) respectively; partial exchange of Al for Si is also possible (Tribaudino et al., 2017). Substitutions are made possible by the rather flexible structure that can accommodate cations with different ionic radii and charges, leading to a wide range of possible compositions (Cameron and Papike, 2018; Papike, 2018).

The chemistry of Mg-Fe-Ca pyroxenes is generally expressed by Mg# (especially for orthopyroxenes, where calcium content is low) and by the percentages of the three end-member compositions: enstatite (En, $MgSiO_3$), ferrosilite (Fe, $FeSiO_3$), and wollastonite (Wo, $CaSiO_3$). Pyroxene crystallizes in monoclinic *C*2/*c* or orthorhombic *Pbca* structure. Orthorhombic pyroxene has the M2 site filled almost completely by Mg and Fe, and the position of Raman peaks is affected by the relative concentration of Mg, Fe, and Ca ions (Wang et al., 2001). In orthopyroxene, the presence of 120 Raman peaks has been predicted, 20-30 of which can be observed in good-quality Raman spectra (Stalder et al., 2009; Stangarone et al., 2016). The small Mg^{2+} ion forms short and strong chemical bonds, leading to higher wavenumber peak positions in the Raman spectrum. Both Fe^{2+} and Ca^{2+} are larger than Mg^{2+}, and their presence shifts the peaks' locations to lower frequencies (Huang, 2000). Numerous studies reported a very good linear correlation between the position of Raman peaks and the Mg# of orthopyroxene (e.g., Mernagh & Hoatson, 1997; Huang et al., 2000; Tribaudino et al., 2012; Andò & Garzanti, 2014; Hu et al., 2015). The greater abundance of the larger Ca^{2+} ion mitigates the effect of the Fe/Mg substitution in the clinopyroxene structure. As Ca and Fe^{2+} substitutions have similar effect, Mg# can thus be more accurately determined by Raman spectroscopy in Ca-poor orthopyroxene (Tribaudino et al., 2011), reaching excellent precision (3.0 and 0.4 weight% for natural and synthetic crystals, respectively; Stalder et al., 2009). By combining the three major peaks of meteoritic and terrestrial orthopyroxene, the Mg/(Mg+Fe+Ca) ratio was measured with an error of only 0.1% (Wang et al., 2001).

The most intense Raman peaks (vibration modes) in the pyroxene spectrum are connected to the vibration of silicate chains bonds, which are unaffected by chemical or structural inhomogeneities (Wang et al., 2001). Most distinctive is the $\nu_3 + \nu_4$ (~655 and ~675 cm^{-1}, respectively) couplet, which is related to the symmetrical bending of the $Si\text{-}O_{bridging}$ bond (i.e., involving the oxygen linking two tetrahedra), and $\nu_5 + \nu_6$ (~1002 and ~1020 cm^{-1}, respectively) couplet, related to the stretching of the $Si\text{-}O_{bridging}$ bond (Makreski et al., 2006; Stangarone et al., 2016). The $\nu_3 + \nu_4$ couplet allows us to discriminate between orthopyroxene and clinopyroxene, the latter showing only one strong narrow peak in this spectral region (with the exception of pigeonite; Tribaudino et al., 2011). The ν_3 and ν_4 vibrational modes are both parallel to the c-axis, and thus independent of crystal orientation (Wang et al., 2001). Instead, the ν_5 and ν_6 vibrational modes are strongly dependent on crystal orientation.

Clusters of medium-intensity Raman peaks also occur in the 300-400 cm^{-1} (M2–O octahedron bending mode) and 510-570 cm^{-1} (O–Si–O bending mode) wavenumber regions (White, 1975; Mernagh & Hoatson, 1997; Huang et al., 2000). Peaks in the < 500 cm^{-1} region are related to M1-O and M2-O crystal-lattice stretching modes (Stangarone et al., 2016); most important to estimate calcium content is the ν_1 (~330 cm^{-1}) vibrational mode (Wang et al., 2001).

3. Sample choice

The choice of samples to be analysed represents the first step to investigate the compositional signatures apt to best discriminate among different types of source rocks in terms of both lithology and geodynamic setting. In this study, we chose to focus on modern sands because a single sediment sample contains a wide spectrum of detrital grains statistically representative of an entire drainage basin, thus offering an efficiency gain relative to techniques focused on bedrock (Greensfelder, 2002). In this way, we could take advantage of decades of quasi-worldwide modern-sand studies and of the collection of over 6000 catalogued sediment samples readily available at the Laboratory for Provenance Studies (University of Milano-Bicocca).

To consider a complete range of lithologies generated and exposed in both orogenic and anorogenic settings, including obduction orogens, continental and arc crust, rift valleys, and continental or intraoceanic volcanic arcs, we selected 15 sand samples from very diverse key regions where source rocks containing significant amounts of orthopyroxene are exposed (Table 1). We thus included mantle harzburgites, lower crustal metagabbros, gabbronorites, and volcanic sequences ranging from andesite to trachyte and dacite, representing different tectono-stratigraphic levels within continental, arc, or oceanic lithosphere.

Structural level	Geodynamic setting	Geological domain	Main lithology	Location
MANTLE	OPHIOLITIC MANTLE	Hatay-Kiziildağ Complex	Harzburgite	Hatay Peninsula (Turkey)
		Sema'il Complex	Harzburgite	Northern Oman Mountains
LOWER CRUST	CONTINENTAL & ARC CRUST	Ivrea-Verbano Mafic Complex	Granulitic gabbro	Southern Alps (Italy)
		Kohistan Arc	Metagabbro to granite	Northern Pakistan
UPPER CRUST	CONTINENTAL MAGMATIC ARC	Andean Cordillera	Andesite and dacite	Río Desaguadero (Argentina)
		Andean Cordillera	Basalt to dacite	Río Grande (Argentina)
		Andean Cordillera	Basalt to dacite	Río Colorado (Argentina)
		Andean Cordillera	Dacite	Río Agrio (Argentina)
	VOLCANIC ARC	Luzon island arc	Basalt to dacite	Taiwan Island
		Kamchatka island arc	Andesite	SE Kamchatcka (Russia)
		Lesser Antilles island arc	Andesite and dacite	Martinique Island
		South Aegean island arc	Andesite and dacite	Santorini Island (Greece)
		Mt. Amiata (Tuscan province)	Trachydacite	Orcia River (Italy)
		Elbrus Volcano	Andesite and dacite	Greater Caucasus (Russia)
	RIFT VALLEY	Virunga volcanic province	K-trachyte and latite	East African Rift (Rwanda)

Table 1. Information on the 15 studied samples of orthopyroxene-rich river and beach sands exclusively or dominantly derived from a range of mantle, deep-crustal, and volcanic rocks generated in different geodynamic settings.

3.1. Ophiolitic mantle

To represent OPX-bearing mantle rocks we have chosen two sand samples, one derived from the Hatay-Kizildağ Ophiolite Complex in southernmost Turkey and one from the Sema'il Ophiolitic Complex in the Northern Oman Mountains.

The Hatay-Kizildağ Complex, a counterpart of the Troodos Complex of Cyprus, is a supra-subduction-zone obducted ophiolite comprising serpentinized mantle rocks overlain by layered gabbros, isotropic gabbros and diorites, sheeted dikes, island-arc tholeiites to boninites, and upper Maastrichtian-Cenozoic cover strata. The 3-km-thick mantle harzburgites containing lenses of dunite, wehrlite, lherzolite and feldspathic peridotite are cross-cut by gabbroic to doleritic dikes (Dilek and Thy, 2009). The Kale beach in the Hatay Peninsula consists of lithic ultramaficlastic sand containing mainly cellular serpentinite and subordinately serpentineschist grains, along with gabbroic rock fragments. The extremely rich tHM (transparent-heavy-mineral) suite is dominated by orthopyroxene associated with olivine (Garzanti et al., 2000).

The Sema'il Ophiolite, also generated in supra-subduction settings at a fast-spreading center around 95 Ma, consists of an 8–12 km-thick section of residual mantle harzburgites, overlain by a 5–8 km-thick crustal section including layered to foliated gabbros, hydrothermally altered diabase dikes, and pillow basalts capped by lower Cenomanian radiolarites (Lippard et al. 1986; Searle and Cox, 1999).

Lithic ultramaficlastic sand of Wadi Dayqat — draining the southern part of the Northern Oman Mountains where mantle rocks are extensively exposed — contains mostly cellular serpentinite and subordinate serpentineschist grains along with significant sedimentary detritus (mostly carbonate grains derived from cover strata), and minor gabbroic and metabasite rock fragments. The rich tHM suite is dominated by orthopyroxene associated with clinopyroxene, olivine, amphibole, and Cr-spinel (Garzanti et al., 2002a).

3.2 Lower continental crust

To represent OPX-bearing gabbroic rocks of the lower continental crust we have chosen one sand sample derived from the Mafic Complex of the Ivrea-Verbano Zone in northern Italy.

The Ivrea-Verbano Zone, the deepest tectonic unit of the Southern Alps, comprises an up to 10 km-thick gabbroic body (Mafic Complex), intruded into high-grade metasediments at a crustal depth of 18–25 km during Early Permian times (Quick et al. 1994). The Mafic Complex includes ultramafic cumulates and layered gabbros, followed by 5–7 km-thick gabbronorite grading upward to monzogabbros and diorites (Rivalenti et al. 1981). Subsolidus re-equilibration under static conditions gave rise to anhydrous assemblages including orthopyroxene, clinopyroxene, and garnet. Retrograde growth of brown amphibole was confined to shear bands within the gabbros (Colombo and Tunesi, 1999).

The plagioclase-dominated sand of the Strona di Postua River contains common gabbroic and a few amphibolite and sillimanite-bearing rock fragments. The extremely rich tHM suite is dominated by orthopyroxene associated with brown amphibole, garnet, and clinopyroxene (Garzanti et al., 2006;

Andò et al., 2014).

3.3. Arc crust

To represent OPX-bearing metamorphic and igneous rocks of deep-seated arc crust we have chosen one sand sample derived from the Kohistan Arc in northern Pakistan.

The Kohistan Batholith represents the dissected remnants of a magmatic arc fed by northward subduction of Neotethyan oceanic lithosphere from Cretaceous to Paleocene times (Searle et al., 1999). The completely exposed 40–50 km-thick lithospheric section includes peridotites and granulite-facies metagabbros at the base, amphibolite and greenschist-facies metasediments intruded by layered gabbronorites, and the gabbroic to granitic rocks of the main calcalkaline batholith overlain by a volcano-sedimentary succession (Jagoutz and Schmidt, 2012).

Plagioclase-rich quartzo-litho-feldspathic sand of the Swat River contains abundant metabasite (epidosite, amphibolite) grains with subordinate metapelite/metapsammite, mafic to felsic plutonic, and serpentinite rock fragments. The extremely rich tHM suite is dominated by blue-green hornblende associated with orthopyroxene, clinopyroxene, and epidote (Garzanti et al., 2005; Liang et al., 2019).

3.4. Continental and island arcs

Two-thirds of the studied samples were selected to provide a relatively wide panorama of subduction-related OPX-bearing volcanic source rocks. Testing areas include east-facing island arcs (Kamchatka Peninsula in eastern Russia and Taiwan Island) and west-facing continental arcs (four samples collected at different latitudes along the Andean Cordillera in Argentina) in the Pacific domain, one east-facing island arc in the Atlantic domain (Martinique Island), one island arc and one continental arc associated with north-eastward and westward subduction in the Mediterranean domain (Santorini Island in Greece and Tuscan Province in Italy, respectively), and the highest volcano in Eurasia (Mt. Elbrus in the Northern Caucasus Range of southern Russia).

3.4.1. Andean cordillera

The Andean continental arc, generated by east-dipping subduction of Paleo-Pacific plates since Jurassic times, consists of N/S-trending belts of mostly granite/granodiorite intrusions and andesite lava flows (Kay et al., 2005). The southern Central Andes (Pampean segment) and northern Southern Andes (Payenia and northern Patagonia segments) exhibit significant along strike variation in subduction angle, degree of tectonic shortening, character and intensity of magmatism, and exposed geological units.

The Pampean flat-slab segment between 27°S and 33°S is characterized by a ~ 600-km-long volcanic gap and comprises a Jurassic–Cenozoic magmatic arc (Cordillera Principal), Carboniferous–Triassic basement uplifts (Cordillera Frontal), a thin-skinned, fold-thrust belt (Precordillera), and the adjacent broken retroarc basin with basement-cored block uplifts (Sierras Pampeanas) (Ramos et al., 2002).

To the south, the Andes are characterized by the active Southern Volcanic Zone emplaced over exhumed Jurassic to Miocene magmatic rocks of the Cordillera Principal, with a thin-skinned belt locally involving basement, and a retroarc basin partitioned by broad and low-relief basement uplifts (Ramos and Kay, 2006). Plio-Quaternary calcalkaline lavas are mostly andesites and dacites, whereas the associated ignimbrites are mostly high-Si andesites, dacites and rhyolites. Orthopyroxene, more abundant than clinopyroxene in dacitic lavas, shows little compositional variation with lava differentiation (Mg# 85-70; Deruelle, 1982).

In the Payenia segment between 34°S and 37°S, extensive Quaternary basaltic fields constitute the largest retroarc mafic volcanic province on Earth (Ramos & Folguera, 2011). Widely distributed throughout the region and spanning from the Cordillera Principal to the retroarc basin are also Upper Carboniferous to Lower Triassic igneous rocks of the Choiyoi Group, including basalts and andesites in the lower part and rhyolitic lavas and ignimbrites in the upper part (Kleiman & Japas, 2009).

In modern sands derived from the eastern slopes of the central and southern Andes in Argentina, orthopyroxene is observed to markedy increase southward from the Pampean flat-slab segment drained by the Río Desaguadero, to the Payenia segment drained by the Río Colorado and its headwater branch Río Grande, and to the northern Patagonia segment drained by the Río Agro (Garzanti et al., 2021a, 2021b). The Río Desaguadero carries feldspatho-litho-quartzose sand with felsic and subordinately intermediate and mafic volcanic grains derived from the Cordillera Prinicpal and Frontal associated with sedimentary and metamorphic rock fragments derived from the Precordillera and Sierras Pampeanas; the moderately poor tHM suite contains clinopyroxene, orthopyroxene, and amphibole in subequal proportions. The Río Grande and Río Colorado carry quartzo-feldspatho-lithic sand with mostly mafic and intermediate volcanic rock fragments and minor sedimentary grains; the rich tHM suite mainly contains clinopyroxene associated with orthopyroxene, brown hornblende and oxy-hornblende, and a few olivine grains. The Río Agro, a branch of Río Negro, carries litho-feldspathic sand dominated by plagioclase displaying spectacular oscillatory zoning associated with mafic and intermediate volcanic rock fragments; the rich tHM suite mostly consists of orthopyroxene with subordinate clinopyroxene and very few olivine and amphibole grains.

3.4.2. Luzon arc

The Luzon intraoceanic arc, fed by the eastward subduction of the Eurasian Plate beneath the Philippine Sea Plate, eventually collided with the Chinese continental margin in the late Miocene, thus starting the growth of the Taiwan doubly-vergent orogenic wedge (Byrne et al., 2011). Luzon Arc remnants are incorporated in the Coastal Range of eastern Taiwan Island, where middle to upper Miocene (15-5 Ma) low-K tholeiitic to medium-K calc-alkaline basaltic to dacitic lava flows and ignimbrites are exposed (Lai et al., 2017).

Feldspatho-lithic sand of the Gaoliao River, draining the western flank of the Chengkuang'ao Volcano, contains mafic and subordinately intermediate volcanic rock fragments, plagioclase, and a few shale/siltstone grains. The very rich tHM suite consists of clinopyroxene and orthopyroxene with a few brown amphibole grains (Garzanti and Resentini, 2016).

3.4.3. Kamchatka arc

The Kamchatka arc lies above a long-lived subduction system. Active volcanoes are numerous in southern Kamchatka, where magmatism is generated by westward subduction of NW Pacific lithosphere beneath the Okhotsk Plate along the Kuril-Kamchatka Trench (Volynets et al., 2010). Among these, the Avachinsky Volcano is characterized by porphyritic basaltic andesite and low-K andesitic lavas and pyroclastic rocks (Viccaro et al., 2012).

Khalaktyrsky beach, situated near Petropavlosk south of the Avachinsky Volcano, consists of plagioclase-dominated feldspatho-lithic sand with mostly mafic and subordinate intermediate volcanic rock fragments. The extremely rich tHM suite consists mainly of orthopyroxene with clinopyroxene and a few olivine and brown amphibole grains (Garzanti and Andò, 2007).

3.4.4. Lesser Antilles arc

The Lesser Antilles island chain is an intraoceanic volcanic arc generated by westward subduction of the Atlantic Plate beneath the Caribbean Plate (Bouysse et al., 1990). Mont Pelée on Martinique Island is a late Quaternary composite andesitic volcano largely made of pyroclastic deposits produced by numerous Plinian, dome-forming, phreatomagmatic, and phreatic eruptions (Germa et al., 2011). Most famous and deadliest was the 1902 eruption, when the city of Saint-Pierre was destroyed by a *nuée ardente* resulting in ~30,000 casualties and very few survivors. Phenocrysts in volcanic rocks are mainly plagioclase displaying oscillatory zoning, associated with olivine and augitic clinopyroxene in basalts, with both clinopyroxene and orthopyroxene in andesites, and with orthopyroxene in dacites (Dupuy et al., 1985).

Saint-Pierre beach, situated south of La Peleé Volcano, consists of plagioclase-dominated litho-feldspathic sand with intermediate and mafic volcanic rock fragments. The extremely rich tHM suite is orthopyroxene-dominated with clinopyroxene and a few brown amphibole grains (Limonta et al., 2015).

3.4.5. South Aegean (Hellenic) arc

The South Aegean volcanic arc is generated by north-eastward subduction of Ionian oceanic lithosphere beneath the extending Greek microplate (Agostini et al., 2010). The most active center is the Santorini island group, built on Mesozoic to Paleogene metapelites and marbles by several large explosive eruptions since ~2 Ma. The Akrotiri Volcanic Complex in the southern part of Thera (the main island) consists of upper Pleistocene (650-550 ka) andesitic to dacitic lavas and younger cinder cones (Druitt et al., 1999).

Red Beach on southern Thera is backed by a 60 m-high, up to 80°-dipping slope of red volcanic rocks subject to high rockfall hazard (Marinos et al., 2017). Its plagioclase-dominated feldspatho-lithic sand consists of mostly mafic and subordinate intermediate volcanic rock fragments. The very rich tHM suite contains clinopyroxene with subordinate orthopyroxene, minor olivine, and a few oxy-hornblende grains (Garzanti and Andò, 2007).

3.4.6. Tuscan magmatic provenance

Westward-subduction beneath the Apennines thrust-belt and opening of the Tyrrhenian back-arc basin triggered extensive late Cenozoic magmatism, with significant contribution of the downgoing Adriatic continental lithosphere to the felsic character of the Tuscan magmatic province (Serri et al. 1993). Mount Amiata in central Italy is a silicic volcano mainly consisting of trachydacitic lavas and pyroclastic products erupted at ~300 ka, followed by trachydacitic and latitic lavas and domes, with a terminal phase characterized by ultrapotassic olivine latite lavas (Ferrari et al., 1996).

The quartz-poor quartzo-lithic sand of the Orcia River, draining the Amiata volcano, mostly consists of carbonate and shale/siltstone rock fragments with only a few and mostly felsic volcanic grains and rare plagioclase. The moderately poor tHM suite is orthopyroxene-dominated with a few clinopyroxene grains (Garzanti et al., 2002b).

3.4.7. Greater Caucasus

The Greater Caucasus marks the northernmost deformation front of the Arabia-Eurasia collision zone, where accelerated exhumation in the central part of the range has been associated with mantle-sourced magmatism since the late Miocene (Vincent et al., 2020). In this region rises the late Quaternary Elbrus stratovolcano, characterized by mainly dacitic lavas and pyroclastic rocks

(Lebedev et al., 2010).
Feldspatho-lithic sand of the Baksan River, draining the southern flank of the Elbrus Volcano, contains intermediate to mafic volcanic grains with zoned plagioclase or pyroxene phenocrysts. Moderately rich tHM suites are orthopyroxene-dominated with oxy-hornblende and only a few clinopyroxene and zircon grains (Vezzoli et al., 2020).

3.5. Continental rifts

As a major difference with respect to subduction-related orogenic lavas, anorogenic volcanic rocks generally lack orthopyroxene. Exceptions however occur. To represent OPX-bearing lavas generated in continental-rift settings we have chosen one sand sample derived from the Virunga volcanic province in Rwanda.
In the western branch of the East African Rift, mainly potassic to ultrapotassic volcanism restricted to accommodation zones between extensional basins initiated at 13-12 Ma and shows a northward increase in alkaline character and CO_2 content (Ebinger and Furman 2003; Pouclet et al., 2016). The Virunga district includes two active volcanoes in Congo and six extinct volcanoes and small cones in Rwanda, where lavas largely erupted in the last 150 ka range from olivine-rich potassic basanites to K-rich or Na-rich trachybasalts. Silica-saturated K-trachytes or latites with orthopyroxene, less titaniferous clinopyroxene, and alkali-feldspar were erupted only from the early Pleistocene Sabinyo Volcano (Rogers et al. 1998).
Feldspatho-lithic sand of the Muhe River, sourced from the Sabinyo Volcano, is dominated by mostly mafic volcanic rock fragments with abundant sanidine microliths set in a glassy groundmass associated with larger calcic plagioclase phenocrysts. The extremely rich tHM suite consists of clinopyroxene and subordinate orthopyroxene, olivine, and rare apatite and epidote (Garzanti et al., 2013).

4. Methods

4.1. Petrographic and heavy-mineral analyses

A quartered fraction of each of the 15 selected sand samples was impregnated with epoxy resin, cut into a standard thin section, and analysed by counting ~400 points according to the Gazzi-Dickinson QFL method (Ingersoll et al. 1984). To collect full information on all rock fragment types and recalculate petrographic parameters according to both Gazzi-Dickinson QFL and traditional QFR methods we used a detailed point-counting sheet that allows the simultaneous registration of the mineral beneath the cross hair and of the rock fragment in which the mineral is located (figure 5 in Garzanti, 2019). Sands were classified according to the proportions of the three main groups of framework components (Q = quartz; F = feldspars; L = lithic fragments; classification scheme after Garzanti, 2019). Median grain size was determined in thin section by ranking and visual comparison with standards of ϕ/4 classes prepared by sieving in our laboratory. From a split aliquot of a conveniently wide size-window obtained by wet sieving (ranging from 63-250 μm to bulk sample for the best sorted sand), heavy minerals were separated by centrifuging in Na-polytungstate (2.90 g/cm^3) and recovered by partial freezing with liquid nitrogen (Andò, 2020). In grain mounts, ≥ 200 transparent heavy minerals for each sample were either grain-counted by the area method or point-counted at appropriate regular spacing to obtain correct volume percentages (Garzanti and Andò 2019). Analyses were carried out by routinely coupling observations under the optical microscope and the Raman spectroscope. Transparent heavy-mineral assemblages, called for brevity "tHM suites" throughout the text, are defined as the spectrum of extrabasinal detrital minerals with density >2.90 g/cm^3 identifiable under a transmitted-light microscope. In the studied samples, their concentration (tHMC) ranges from moderately poor to extremely rich (1-2% and > 20% of total extrabasinal detritus). Full information on samples and sampling sites, and the complete petrographic and heavy-mineral datasets are provided in Appendix Tables A1, A2, and A3, respectively.

4.2. Optical and Raman spectroscopy analyses

For each of the 15 studied samples another split aliquot of the separated > 2.90 g/cm^3 fraction was mounted on Huntsman Araldite® DBF resin and polished. On photographic maps of the mounts, each pyroxene grain was labelled by a progressive number. On each sample, a preliminary investigation on numerous orthopyroxene grains selected at random was carried out under a polarized Leica DM750 microscope, and the main optical features (i.e., colour, pleochroism, habit, z/c angle, birefringence, elongation, interference figures, optical sign) were recorded for 458 grains overall.

Taking care to avoid inclusions and weathering patinas, 500 Raman spectra overall were collected with a high-resolution Renishaw inVia™ equipped with a Leica DM2500 polarizing microscope and motorized x-y stages, using a 50×LWD (long working distance) objective, a solid-state 532 nm laser, and a grating of 1800 lines/mm in the 140–1900 cm^{-1} range. Acquisition time was ~40 s, space resolution < 5 μm, spectral resolution ± 0.5 cm^{-1}, and power ≤ 10 mW at the sample. Calibration was done before each experimental session with a silicon wafer standard (peak at 520.7 cm^{-1}). To expand the dataset and test its quality and reliability, 40 grains from different samples and characterised by diverse Mg# were investigated at the University of Parma with a high-resolution

Horiba LabRam HR Evolution confocal micro-spectrometer (800 mm focal length) equipped with an Olympus BX41 microscope and x-y-z motorized stage using a 100× objective, a He-Ne (632.8 nm) laser, and a 600 groves/mm blazed grating. Acquisition time was 50 s, space resolution ~1 µm, spectral resolution better than 0.5 cm^{-1}. Full widths at half maximum (FWHM) were measured on these high-resolution spectra.

The software LABSPEC 5 (Horiba Ltd.) was used for baseline subtraction. Peak positions were measured by the Gaussian–Lorentzian (pseudo-Voigt) deconvolution method, reaching an accuracy of ± 0.3 cm^{-1}. The results of Raman analyses are provided in Appendix Tables A4 and A5.

4.3. SEM-EDS minerochemistry

The 15 grain mounts were coated with graphite and over 600 analyses were made at the SEM-EDS (scanning electron microscopy-energy dispersive spectrometer), exactly on the same spot analysed by Raman spectroscopy, on 350 selected grains yielding higher, medium, and lower frequency Raman peaks reflecting higher, medium, and lower Mg content. By combining observations of the very same grains at the optical microscope, Raman spectroscope, and scanning electron microscope we could thus compare and confidently correlate optical properties, position of Raman peaks, and chemical compositions of 350 orthopyroxene grains.

Minerochemical analyses were carried out at the University of Milano-Bicocca with a TESCAN VEGA TS Univac 5136 XM set with a EDAX GENESIS 4000 XMS Imaging 60 SEM electronic microprobe, under an electron beam of 20-kV high voltage, 250-nm spot size, 45° take-off angle, and current absorption 190±1 pA, measured in platinum Faraday cup. The quantification of main elements (Mg, Fe, Ca, Na, Si, and Al) was calibrated with Astimex Scientific standards. Compositions were calculated using PX-NOM software (Sturm, 2002) following the nomenclature of Morimoto et al. (1988). The complete dataset of SEM-EDS analyses is provided in Appendix Tables A6 and A7.

5. Results

5.1. Optical observations

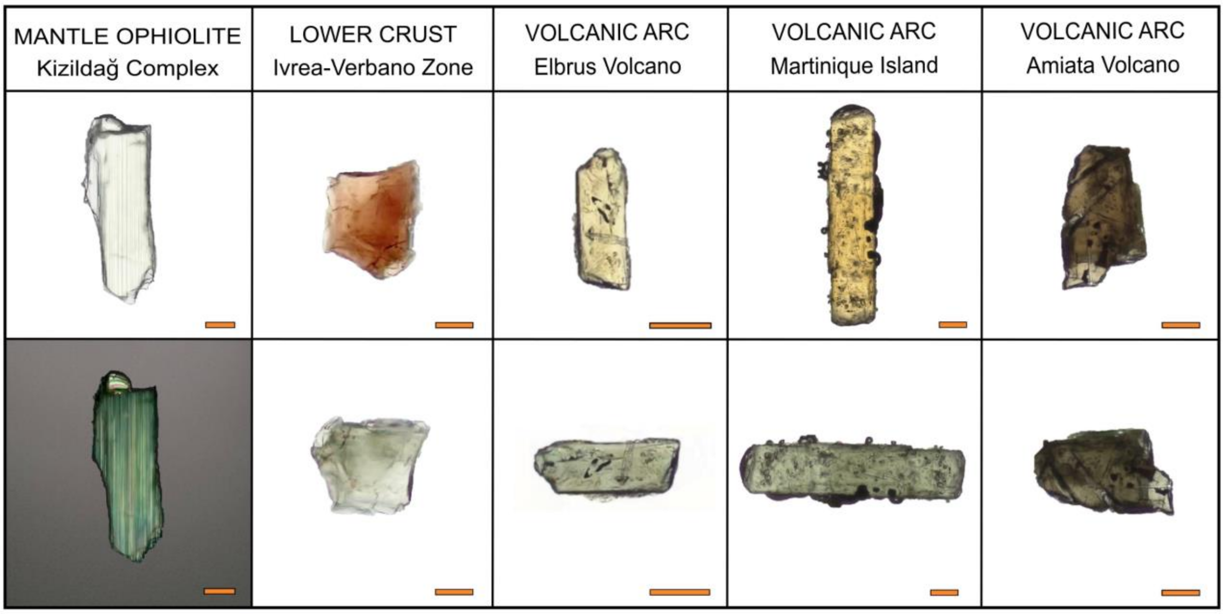

Figure 2. Typical optical features displayed by orthopyroxene grains derived from mantle, lower crustal, and volcanic rocks. Enstatite *s.s.* from the Kizildağ harzburgite is shown both at parallel and crossed polarizers, whereas other orthopyroxenes are rotated by 90° to show their characteristic pleochroism. Scale bar: 100 μm.

Under the polarized microscope, virtually colourless and optically positive enstatite *s.s.*, which dominates the tHM assemblage of the two sands derived from the Kizildağ and Sama'il mantle harzburgites where it commonly contains exsolution lamellae of clinopyroxene (Fig. 2), is readily distinguished from pleochroic hypersthene *s.l.*, which is dominant in all other samples. Pleochroism intensity and colour vary depending on the observed crystal face: only the {100} face − most commonly observed in grain mounts − shows strong pleochroism with yellow to pink *versus* green shades, whereas the {010} face displays only greenish shades (Tröger, 1979; Mange and Maurer, 1992). Pleochroism is a complex phenomenon variously ascribed to: i) iron content and ordering; ii) presence of Ti, Mn, Cr, Ni, or Al ions; iii) oriented inclusions and lamellae; iv) Al-driven lattice distortion (Kuno, 1954; Burns, 1966).

In this study, we failed to see a clear correlation between Mg# and pleochroism intensity, and noticed numerous Fe-rich orthopyroxene grains showing weak colour. Most evident is the difference in pleochroism between yellow-orange/green orthopyroxene derived from effusive volcanic rocks and pink-reddish/green orthopyroxene derived from deep-crustal Ivrea-Verbano and Kohistan intrusive rocks (Jan and Howie, 1980) (Fig. 2).

5.2. SEM–EDS minerochemical data

Geodynamic setting	Unit		SiO_2 wt%	TiO_2 wt%	Al_2O_3 wt%	FeO wt%	MnO wt%	MgO wt%	CaO wt%	K_2O wt%	Na_2O wt%	Cr_2O_3 wt%	Mg#	En mol%	Fe mol%	Wo mol%
OPHIOLITIC MANTLE	Kiziildağ	**Mean**	**56.6**	**b.d.l.**	**2.0**	**5.6**	**0.02**	**33.8**	**1.5**	**b.d.l.**	**b.d.l.**	**0.8**	**0.92**	**88.9**	**8.3**	**2.9**
		Max	57.3	b.d.l.	2.5	5.9	0.2	34.5	2.3	b.d.l.	b.d.l.	1.0	0.96	89.9	8.7	4.2
		Min	*56.0*	*b.d.l.*	*1.6*	*5.2*	b.d.l.	*33.2*	*0.9*	*b.d.l.*	*b.d.l.*	*0.6*	*0.91*	*88.1*	*7.7*	*1.6*
	Sema'il	**Mean**	**55.4**	**0.3**	**2.2**	**6.8**	**0.3**	**32.2**	**1.2**	**0.1**	**0.3**	**1.1**	**0.91**	**87.0**	**10.7**	**2.3**
		Max	56.6	0.4	3.3	8.8	0.4	33.3	2.1	0.3	0.4	1.4	0.94	88.4	13.9	4.1
		Min	*54.3*	*0.2*	*0.8*	*5.8*	*0.2*	*31.6*	*0.6*	b.d.l.	*0.08*	*0.7*	*0.87*	*84.9*	*9.3*	*1.1*
CONTINENTAL & ARC CRUST	Ivrea-Verbano	**Mean**	**52.6**	**0.02**	**2.4**	**21.4**	**0.6**	**22.2**	**0.5**	**b.d.l.**	**0.02**	**b.d.l.**	**0.65**	**63.4**	**35.5**	**1.1**
		Max	54.9	0.2	3.6	27.4	0.8	26.5	0.8	b.d.l.	0.2	b.d.l.	0.75	72.9	46.4	1.7
		Min	*51.3*	*b.d.l.*	*1.6*	*16.3*	*0.4*	*17.6*	*0.4*	*b.d.l.*	b.d.l.	*b.d.l.*	*0.53*	*51.9*	*26.1*	*0.9*
	Kohistan	**Mean**	**51.5**	**b.d.l.**	**1.7**	**24.3**	**0.5**	**20.4**	**0.8**	**b.d.l.**	**b.d.l.**	**b.d.l.**	**0.61**	**58.5**	**40.0**	**1.6**
		Max	52.7	b.d.l.	2.2	25.9	0.8	21.4	1.1	b.d.l.	b.d.l.	b.d.l.	0.63	60.7	43.3	2.4
		Min	*50.9*	*b.d.l.*	*1.0*	*23.1*	*0.3*	*18.7*	*0.4*	*b.d.l.*	*b.d.l.*	*b.d.l.*	*0.57*	*54.3*	*37.6*	*0.7*
CONTINENTAL MAGMATIC ARC	Río Desaguadero (Argentina)	**Mean**	**53.9**	**0.6**	**1.2**	**18.0**	**0.3**	**24.5**	**1.6**	**0.2**	**0.3**	**0.02**	**0.73**	**68.3**	**28.5**	**3.2**
		Max	56.2	0.8	2.7	21.1	0.5	30.8	2.0	0.4	0.5	0.5	0.88	82.9	33.7	4.2
		Min	*52.3*	*0.3*	*0.5*	*9.7*	*0.1*	*22.2*	*1.0*	*0.06*	*0.1*	b.d.l.	*0.66*	*63.5*	*14.8*	*2.0*
	Río Grande (Argentina)	**Mean**	**54.7**	**0.5**	**0.9**	**17.1**	**0.4**	**23.2**	**1.5**	**0.2**	**0.4**	**b.d.l.**	**0.69**	**66.7**	**30.2**	**3.1**
		Max	55.8	0.7	1.6	21.4	0.6	25.5	1.9	0.3	0.8	b.d.l.	0.74	71.7	35.4	3.9
		Min	*53.5*	*0.3*	*0.2*	*15.7*	*0.2*	*21.1*	*1.0*	*0.1*	*0.2*	*b.d.l.*	*0.64*	*61.3*	*25.2*	*2.2*
	Río Colorado (Argentina)	**Mean**	**53.9**	**0.2**	**0.7**	**18.6**	**0.9**	**24.1**	**1.6**	**b.d.l.**	**0.3**	**0.02**	**0.71**	**66.7**	**30.3**	**3.1**
		Max	55.1	0.4	1.3	22.0	1.7	26.3	2.4	b.d.l.	0.6	0.3	0.80	71.3	35.6	4.8
		Min	*53.1*	*0.1*	*0.5*	*15.4*	*0.5*	*21.5*	*1.1*	*b.d.l.*	*0.2*	b.d.l.	*0.65*	*61.4*	*24.3*	*2.2*
	Río Agrio (Argentina)	**Mean**	**53.0**	**0.4**	**0.7**	**24.8**	**0.6**	**18.8**	**1.5**	**b.d.l.**	**0.3**	**b.d.l.**	**0.58**	**55.1**	**41.7**	**3.2**
		Max	54.9	0.7	2.4	27.0	1.1	24.8	2.0	b.d.l.	0.8	b.d.l.	0.74	71.2	44.2	4.2
		Min	*50.7*	*0.2*	*0.3*	*15.3*	*0.3*	*17.5*	*1.3*	*b.d.l.*	*0.05*	*b.d.l.*	*0.55*	*52.9*	*25.1*	*2.5*
VOLCANIC ARC	Taiwan	**Mean**	**53.2**	**0.4**	**1.2**	**18.2**	**0.5**	**24.8**	**1.5**	**0.1**	**0.2**	**0.3**	**0.73**	**68.2**	**28.9**	**2.9**
		Max	54.2	0.5	1.7	20.1	0.7	27.5	2.0	0.2	0.4	0.5	0.83	74.9	31.7	3.8
		Min	*52.0*	*0.2*	*0.7*	*13.4*	b.d.l.	*23.6*	*0.8*	b.d.l.	*0.09*	b.d.l.	*0.70*	*65.4*	*21.2*	*1.6*
	Kamchatka	**Mean**	**52.5**	**0.4**	**1.4**	**17.9**	**0.4**	**25.0**	**1.6**	**0.2**	**0.2**	**0.09**	**0.75**	**68.7**	**28.2**	**3.1**
		Max	53.5	0.6	2.4	21.1	0.7	26.3	2.0	0.3	0.4	0.2	0.80	71.7	34.2	4.0
		Min	*51.5*	*0.3*	*0.6*	*15.9*	*0.2*	*22.7*	*1.0*	*0.04*	*0.1*	b.d.l.	*0.68*	*63.5*	*24.6*	*2.1*
	Martinique	**Mean**	**50.5**	**0.4**	**0.9**	**26.1**	**1.2**	**19.4**	**1.4**	**b.d.l.**	**0.2**	**0.3**	**0.61**	**54.2**	**43.0**	**2.8**
		Max	53.4	0.7	1.8	29.4	1.5	21.9	1.6	b.d.l.	0.4	0.5	0.69	59.3	48.1	3.2
		Min	*48.4*	*0.2*	*0.3*	*23.5*	*0.8*	*17.3*	*0.9*	*b.d.l.*	b.d.l.	*0.1*	*0.53*	*49.2*	*37.7*	*1.7*
	Santorini	**Mean**	**51.0**	**0.4**	**0.8**	**22.7**	**0.9**	**22.4**	**1.6**	**0.1**	**0.2**	**0.01**	**0.66**	**59.9**	**36.9**	**3.2**
		Max	53.6	0.6	1.3	26.7	1.4	43.5	2.2	0.2	0.3	0.07	0.72	66.4	44.9	4.4
		Min	*50.7*	*0.3*	b.d.l.	*16.1*	*0.3*	*18.2*	*0.4*	*0.05*	b.d.l.	b.d.l.	*0.58*	*52.1*	*19.2*	*0.5*
	Amiata	**Mean**	**49.8**	**0.4**	**0.6**	**32.0**	**0.4**	**14.7**	**1.5**	**0.2**	**0.1**	**b.d.l.**	**0.47**	**43.3**	**53.6**	**3.1**
		Max	51.5	0.7	1.4	35.0	0.7	17.0	1.8	0.4	0.4	b.d.l.	0.54	49.3	57.9	3.7
		Min	*48.5*	b.d.l.	b.d.l.	*28.6*	*0.2*	*13.2*	*1.1*	b.d.l.	b.d.l.	*b.d.l.*	*0.41*	*38.9*	*47.3*	*2.4*
	Elbrus	**Mean**	**54.2**	**0.4**	**1.3**	**17.2**	**0.5**	**25.7**	**1.3**	**b.d.l.**	**b.d.l.**	**0.2**	**0.73**	**70.2**	**27.3**	**2.5**
		Max	55.1	0.4	2.6	21.7	0.8	29.0	1.6	b.d.l.	b.d.l.	0.5	0.81	77.7	34.9	3.1
		Min	*52.8*	*0.2*	*0.5*	*12.5*	*0.3*	*22.9*	*1.0*	*b.d.l.*	*b.d.l.*	b.d.l.	*0.65*	*63.3*	*19.2*	*1.9*
RIFT VALLEY	Virunga	**Mean**	**52.1**	**0.5**	**0.9**	**22.3**	**0.2**	**20.9**	**1.6**	**b.d.l.**	**0.2**	**0.2**	**0.63**	**60.2**	**36.4**	**3.4**
		Max	52.9	0.5	1.1	25.6	0.3	22.8	1.8	b.d.l.	0.3	0.3	0.69	64.8	42.1	3.6
		Min	*51.4*	*0.4*	*0.5*	*19.7*	*0.2*	*18.7*	*1.5*	*b.d.l.*	*0.2*	b.d.l.	*0.57*	*54.6*	*31.8*	*3.2*

Table 2. Chemical composition of detrital othopyroxenes analyzed by SEM-EDS. Note high Si and Cr in Mg-rich OPX from mantle rocks and low Ca in OPX from lower-crustal Ivrea-Verbano metagabbros and Kohistan arc intrusives; all these OPX are Ti-poor. Fe-rich OPX from Mt. Amiata is poor in Si and Al. No distinctive features are displayed by OPX from Virunga trachytes. Mg#: Mg/(Mg+Fe) atomic ratio; En: enstatite; Fs: ferrosilite; Wo: wollastonite; b.d.l.: below detection limit.

As anticipated (e.g., Dilek & Newcomb, 2003), detrital orthopyroxene from mantle rocks yielded much higher Cr (0.9±0.2 wt% Cr_2O_3) and Mg concentrations (Mg# 0.92±0.02; En 88±1) than all other samples ($Cr_2O_3 \leq 0.5$ wt%; Mg# 0.67±0.07; En 63±7). SiO_2 is also high, whereas TiO_2 is low (Table 2). Mg# is highest in Kizildağ-derived sand and Cr highest in the Sama'il-derived sand (Fig. 3).

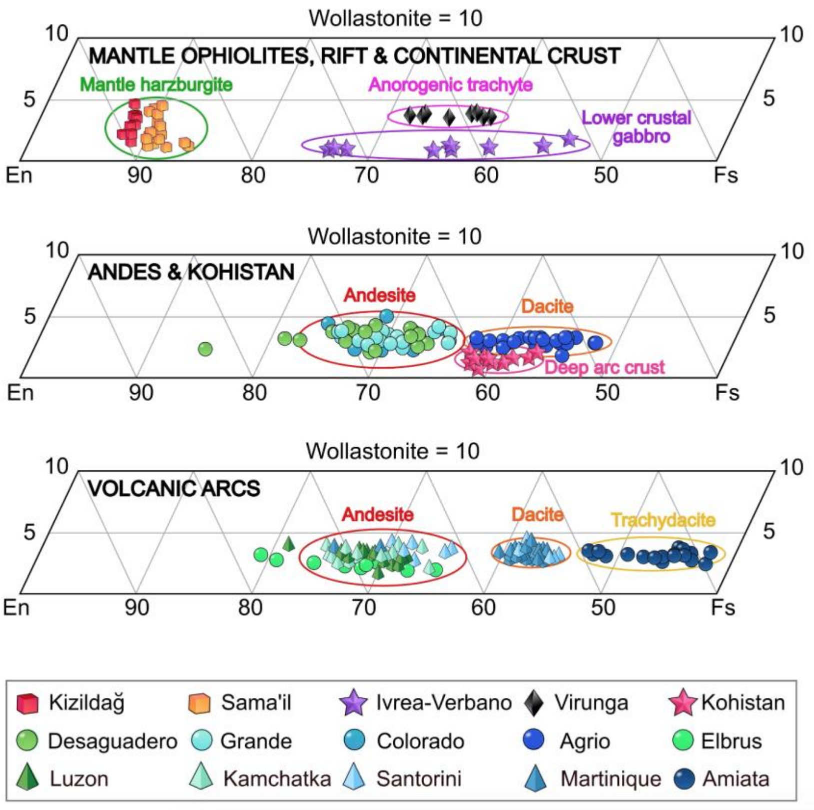

Figure 3. Chemical composition of detrital othopyroxenes determined by SEM-EDS. The 350 analyzed grains from 15 sand samples provide a statistical representation of a range of source-rock lithologies at different structural levels of continental crust, arc crust, and oceanic lithosphere. Only a few grains yielded En values between 85 and 75. En: enstatite; Fs: ferrosilite; Wo: wollastonite. Colour codes similar as in Fig. 6.

Detrital orthopyroxenes from lower-crustal Ivrea-Verbano granulitic metagabbros and Kohistan intrusive rocks are singled out by their calcium content, notably lower (Wo 1.3±0.4%) than both mantle-derived (Wo 2.4±0.9) and volcanic-derived orthopyroxene (Wo 3.1±0.6%). It must be noted, however, that Ca determination by SEM-EDS may be influenced by the presence of clinopyroxene or plagioclase impurities (Lindh, 1975). Ivrea-Verbano orthopyroxenes show two populations (Mg# 73-71 and 64-52), whereas Kohistan orthopyroxenes are tightly clustered (Mg# 0.61±0.2) (Fig. 3). TiO_2 is also low (Table 2).

Detrital orthopyroxene in the 10 studied sands derived from intraoceanic to continental volcanic arcs yielded compositions ranging widely from Mg# 80 to Mg# 40, broadly showing three clusters. The main cluster centered at Mg# 70 comprises orthopyroxene grains derived from andesites of the Andean Cordillera and carried by the Desaguadero, Grande, and Colorado Rivers. Slightly richer in Mg are orthopyroxenes from the Luzon Arc in Taiwan, Elbrus Volcano in the Greater Caucasus, and Avachinsky Volcano in Kamchatka, and the few richest Mg-rich grains (Mg# 80-75) were found in Desaguadero, Colorado, Elbrus, Kamchatcka, and Taiwan sands (Fig. 3). A second main cluster centered at Mg# 55 comprises orthopyroxene grains derived from dacites of the Andean Cordillera and carried by the Agrio River or found in the Saint Pierre beach on Martinique Island. Both of these two main clusters are represented in the Red beach on Santorini Island (Fig. 3). A third cluster (Mg# 50-40) is defined by the Fe-rich orthopyroxene grains shed by the trachydacites of the Amiata Volcano in Tuscany, which are poor in SiO_2 and Al_2O_3 (Table 2).

Detrital orthopyroxene from the rift-related Virunga trachytes (Mg# 0.62±0.03; En 60±3) can hardly be distinguished from grains shed by volcanic arcs, although they tend to have slightly more Ca (Wo 3.5±0.3) (Fig. 3).

According to the traditional classification (Poldervaart, 1947), orthopyroxene grains from the Kizildağ harzburgites (En 90-88) will all classify as enstatite, whereas some grains from Sema'il harzburgites (En 88-85) turned out to be magnesium-rich bronzites despite their very similar optical properties (Fig. 2). Iron-rich bronzites (Mg# 0.8-0.7) are the most common orthopyroxene in Kamchatka, Elbrus and Taiwan sands and are as common as magnesium-rich hypersthene (Mg# 0.7-0.6) in most Andean samples (Desaguadero, Grande, and Colorado Rivers). Hypersthene is prevalent in Ivrea-Verbano sand derived from lower crustal metagabbros and dominant in Kohistan sand derived from arc intrusives as in Virunga sand derived from rift-related trachytes. Hypersthene with bimodal composition (Mg# 0.7-0.65 and 0.6-0.55) characterizes Santorini beach sand. Low-magnesium hypersthene (Mg# 0.6-0.55) dominates Agrio sand from dacites of the Andean Cordillera. Fe-hypersthene is found and dominant only in sand from the silicic Amiata Volcano.

SEM-EDS analyses also highlighted the relationships among the concentrations of diverse chemical elements in orthopyroxene. This issue was investigated by Howie and Smith (1966), who found that Mg# correlates well with Cr, Ni and Al, anticorrelates with Ca and Mn, and is uncorrelated with Ti. In the 350 analysed detrital orthopyroxenes, Mg# correlates positively with SiO_2 (*r* 0.70), Al_2O_3 (*r* 0.58), and Cr_2O_3 (*r* 0.62), whereas no correlation was observed with CaO (Fig. 4). TiO_2 correlates with CaO (*r* 0.60), K_2O (*r* 0.44), and Na_2O (*r* 0.37). MnO correlates weakly positively with FeO (*r* 0.33) and negatively with all other elements. Al_2O_3 correlates weakly negatively with CaO (*r* 0.38).

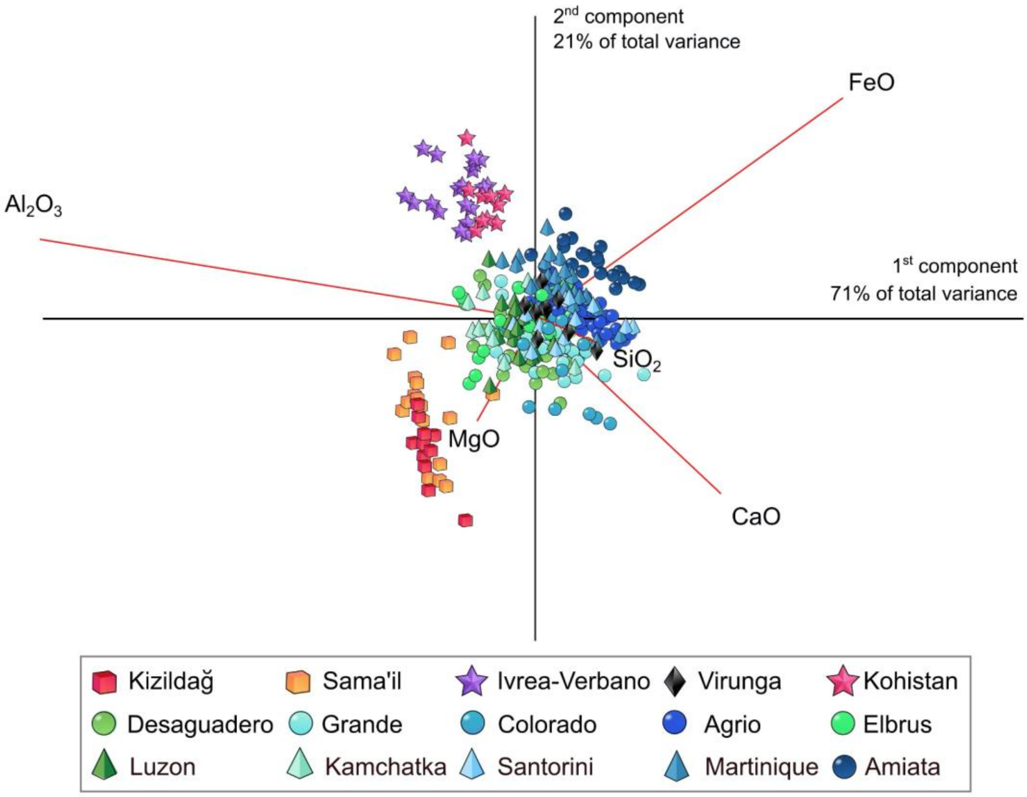

Figure 4. Relationships among major chemical elements hosted in detrital orthopyroxenes as determined by SEM-EDS. OPX from mantle harzburgites is highest in Mg, OPX from lower continental and arc crust poorest in Ca. Volcanic OPX, poorer in Al, displays decreasing Mg# from andesite to dacite and more felsic source rocks. Arc and rift-related volcanic OPX are not different. The biplot (Gabriel, 1971) drawn using CoDaPack software by Comas-Cufí and Thió-Henestrosa, 2011) displays multivariate observations (points) and variables (rays). The length of each ray is proportional to the variance of each element in the dataset. If the angle between two rays is close to 0°, 90°, and 180°, then the corresponding compositional parameters are directly correlated, uncorrelated, and inversely correlated, respectively. Colour codes similar as in Fig. 6.

6. Raman spectroscopy analysis of orthopyroxene

A main goal of this study was to provide a robust time-saving method to estimate Mg# and thus distinguish among several orthopyroxene compositions during routine provenance analysis. About 500 Raman spectra were collected, 350 of which were related to the chemical composition.

After baseline subtraction and deconvolution (Fig. 5), all peak positions were reported in Excel™ sheets. The 300-400 cm^{-1} cluster was considered as the sum of four vibrational modes (ν_1 and ν_2 being those with the lowest and highest frequencies). The six most intense and clearly distinguishable peaks were considered for Mg# estimation (Table 3): ν_1 (~ 330 cm^{-1}); ν_2 (~ 395 cm^{-1}); ν_3 (~ 655 cm^{-1}); ν_4 (~ 675 cm^{-1}); ν_5 (~ 1002 cm^{-1}); and ν_6 (~ 1020 cm^{-1}). Plots in Fig. 6 permit an accurate correlation among vibrational modes and Mg content in orthopyroxene, thus allowing a ready estimate of Mg# during routine provenance analysis.

Geodynamic setting	Unit	Mg#		ν_1 cm^{-1}	ν_2 cm^{-1}	ν_3 cm^{-1}	ν_4 cm^{-1}	ν_5 cm^{-1}	ν_6 cm^{-1}
OPHIOLITIC MANTLE	Kiziildağ	**0.92**	**Mean**	**343.4**	**400.8**	**662.1**	**683.8**	**1011.5**	**1030.1**
		0.96	Max	344.3	402.3	662.7	684.6	1012.9	1031.0
		0.91	*Min*	*342.1*	*398.5*	*661.4*	*683*	*1010.1*	*1028.4*
	Sema'il	**0.91**	**Mean**	**343.5**	**400.5**	**661.9**	**683.9**	**1010.3**	**1030.5**
		0.94	Max	345.0	403.8	662.8	684.9	1012.6	1033.1
		0.87	*Min*	*341.2*	*397.8*	*661.2*	*683.3*	*1009.7*	*1027.1*
CONTINENTAL & ARC CRUST	Ivrea-Verbano	**0.65**	**Mean**	**335.9**	**393.6**	**654.8**	**675.6**	**1000.1**	**1014.6**
		0.75	Max	340.8	402.1	658.0	679.4	1004.2	1022.1
		0.53	*Min*	*332.5*	*384.2*	*652.4*	*672.1*	*996.7*	*1007.0*
	Kohistan	**0.61**	**Mean**	**334.7**	**389.8**	**654.6**	**674.3**	**999.3**	**1013.6**
		0.63	Max	336.7	399.2	656.2	676.0	1001.0	1021.1
		0.57	*Min*	*332.2*	*382.0*	*652.7*	*672.5*	*997.6*	*1009.4*
CONTINENTAL MAGMATIC ARC	Río Desaguadero (Argentina)	**0.73**	**Mean**	**333.7**	**394.4**	**656.1**	**675.8**	**1003.8**	**1021.9**
		0.88	Max	340.9	401.1	660.0	681.6	1007.8	1030.5
		0.66	*Min*	*331.0*	*387.3*	*654.1*	*673.5*	*1001.5*	*1016.8*
	Río Grande (Argentina)	**0.69**	**Mean**	**331.8**	**393.0**	**655.3**	**674.6**	**1002.9**	**1019.9**
		0.74	Max	335.7	397.4	657.4	676.6	1005.2	1024.4
		0.64	*Min*	*326.6*	*387.9*	*652.8*	*672.0*	*1000.3*	*1016.3*
	Río Colorado (Argentina)	**0.71**	**Mean**	**332.9**	**394.5**	**655.9**	**675.3**	**1003.1**	**1018.2**
		0.80	Max	335.1	403.4	657.7	677.2	1005.0	1022.9
		0.65	*Min*	*330.5*	*390.0*	*654.3*	*673.3*	*1001.2*	*1012.8*
	Río Agrio (Argentina)	**0.58**	**Mean**	**329.6**	**390.2**	**653.3**	**672.5**	**1000.9**	**1015.1**
		0.74	Max	336.4	397.6	656.8	677.5	1005.2	1023.4
		0.55	*Min*	*328.4*	*386.8*	*652.6*	*671.6*	*999.8*	*1010.4*
VOLCANIC ARC	Taiwan	**0.73**	**Mean**	**333.8**	**395.0**	**656.4**	**676.2**	**1003.6**	**1019.7**
		0.83	Max	336.2	399.5	658.2	678.1	1006.5	1024.9
		0.70	*Min*	*326.4*	*392.4*	*655.5*	*675.1*	*1002.3*	*1011.0*
	Kamchatka	**0.75**	**Mean**	**333.5**	**393.8**	**656.0**	**675.7**	**1003.6**	**1021.9**
		0.80	Max	336.3	398.0	657.4	677.4	1005.9	1026.3
		0.68	*Min*	*329.0*	*389.3*	*653.0*	*673.2*	*1001.4*	*1016.4*
	Martinique	**0.61**	**Mean**	**329.9**	**390.5**	**653.6**	**672.3**	**1000.0**	**1014.9**
		0.69	Max	332.8	397.4	655.1	674.0	1001.7	1019.8
		0.53	*Min*	*328.0*	*385.7*	*652.0*	*670.9*	*998.3*	*1011.8*
	Santorini	**0.66**	**Mean**	**330.8**	**392.1**	**654.2**	**673.4**	**1001.8**	**1018.4**
		1.00	Max	334.2	402.4	660.8	676.6	1006.7	1022.8
		0.58	*Min*	*327.9*	*386.9*	*651.4*	*670.8*	*999.7*	*1013.8*
	Amiata	**0.47**	**Mean**	**324.9**	**384.8**	**650.0**	**668.7**	**996.6**	**1010.4**
		0.54	Max	328.3	395.3	651.7	670.2	997.5	1016.9
		0.41	*Min*	*322.1*	*377.1*	*648.9*	*667.5*	*995.8*	*1001.4*
	Elbrus	**0.73**	**Mean**	**333.5**	**395.7**	**655.9**	**675.8**	**1002.6**	**1019.5**
		0.81	Max	339.1	400.9	659.3	680.0	1006.5	1024.9
		0.65	*Min*	*326.7*	*387.7*	*652.6*	*671.9*	*999.7*	*1008.2*
RIFT VALLEY	Virunga	**0.63**	**Mean**	**331.1**	**390.8**	**654.1**	**673.1**	**1000.9**	**1016.7**
		0.69	Max	332.5	395.7	655.6	674.6	1004.5	1021.6
		0.57	*Min*	*328.9*	*386.8*	*652.5*	*671.7*	*999.2*	*1012.6*

Table 3. Mean, minimum and maximum Raman peak positions (vibrational modes ν1 to ν6) distinctive of detrital othopyroxene derived from a range of mantle, deep crustal, and volcanic rocks representing different geodynamic settings. Mg#: Mg/(Mg+Fe) atomic ratio.

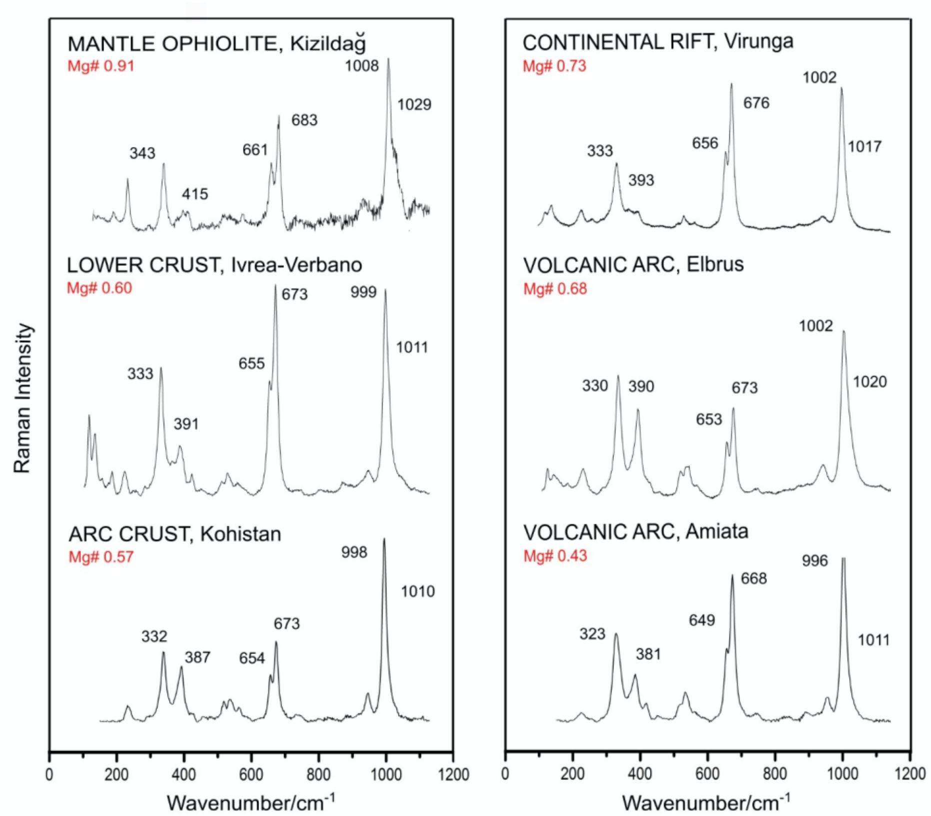

Figure 5. Selected Raman spectra of orthopyroxene grains from diverse source rocks in different geodynamic settings. Baseline subtraction was obtained with Labspec 5 software. Greater background noise for Cr-rich harzburgite-derived OPX is ascribed to Cr-induced fluorescence (Savel'eva et al., 2013). Peaks are stronger for more ordered OPX derived from lower-crustal granulitic metagabbro. In the low-wavelength spectral region, peaks' shape and relative intensity depends on crystal orientation.

As previously documented (e.g., Wang et al., 2001; Stalder et al., 2009), Raman peak positions are linearly correlated to Mg content (right panels in Fig. 6) and one to the other (selected peak combinations are shown in left panels of Fig. 6). Six formulas to calculate Mg content from peak frequencies were thus obtained (Table 4).

Vibrational modes	Equations (cm^{-1})	R^2	σMg#
v_1 (~ 330 cm^{-1})	Mg# = **(v_1** – 309.0) / 34.9	0.8	0.19
v_2 (~ 395 cm^{-1})	Mg# = **(v_2** – 372.0) / 31.3	0.52	0.31
v_3 (~ 655 cm^{-1})	Mg# = **(v_3** – 639.5) / 23.2	0.88	0.15
v_4 (~ 675 cm^{-1})	Mg# = **(v_4** – 655.1) / 29.2	0,88	0.13
v_5 (~ 1002 cm^{-1})	Mg# = **(v_5** – 984.5) / 26.5	0.85	0.16
v_6 (~ 1020 cm^{-1})	Mg# = **(v_6** – 989.9) / 42.4	0.72	0.21

Table 4. Mg# calculated from Raman peak positions. R^2 and σMg# represent the proportion of the variation and expected uncertainty when Mg# is derived from the value of a single Raman peak.

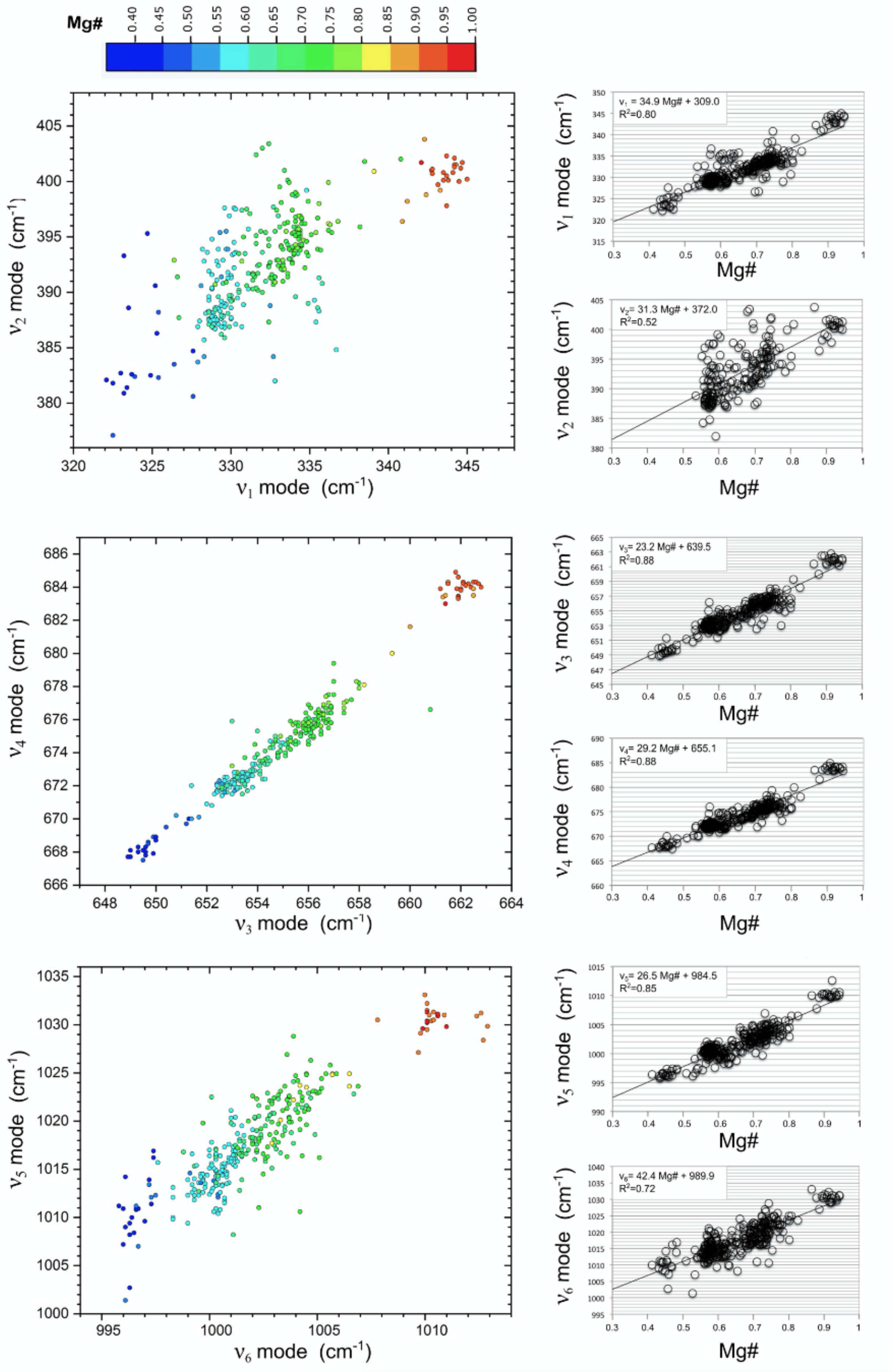

Figure 6. Sensitivity of Raman peak positions to Mg# in detrital orthopyroxene as determined by SEM-EDS. The best correlation between peak position and Mg# is obtained for vibrational modes ν3 and ν4, which display excellent linear correlation with each other (middle panel to the right). Among other peaks, ν_1, ν_5, and ν_6 can be used to increase the accuracy of Mg# determination, whereas ν_2 is least reliable. Colour scale reflects decreasing Mg# from red (Mg# 1.0) to blue (Mg# 0.4).

The correlation is strongests for ν_1, ν_3, ν_4, and ν_5 and weaker for ν_2 and ν_6, largely because of their lower intensity and consequent difficulty in the deconvolution and precise assessment of peak frequencies. The intense narrow couplet around 660 cm^{-1} thus allowing a very accurate measure of both band positions is the most reliable for Mg# estimation. A good correlation between Mg content and peak locations is also hampered by the variable amount of calcium, which in the studied grains is lower in continental and arc crust orthopyroxenes (Ivrea Verbano and Kohistan) than in the other samples. For this reason, Huang et al. (2000) proposed two different formulas for Ca-rich and Ca-poor orthopyroxene, obtaining a lower error. Calcium content, however, must be known beforehand. Because ν_1 correlates negatively with calcium content (Tribaudino et al., 2012; Stangarone et al., 2016), Ca-poor Ivrea Verbano and Kohistan orthopyroxenes plot above the wavenumber/Mg# regression line for the ν_1 (~ 330 cm^{-1}) peak, resulting in higher frequencies for the same Mg/Fe ratio. Among other peaks, only ν_5 is slightly sensitive to calcium content. No correlation with Al content was found.

Full widths at half maximum (FWHM) for all six vibrational modes were measured to test the potential of Raman analysis to distinguish between volcanic and highly ordered metamorphic orthopyroxenes (Ghose and Hafner, 1967). No significant difference, however, was observed among orthopyroxene shed by mantle ophiolites, lower crustal metagabbros, and volcanic rocks.

7. Provenance implications

This study was aimed at testing whether orthopyroxene grains derived from a range of source-rock lithologies belonging to different tectono-stratigraphic levels and generated in different geodynamic settings have sufficiently distinct chemical composition to be distinguished by Raman spectroscopy during provenance analysis.

Several previous studies were dedicated to discriminate orthopyroxene hosted in intrusive *versus* metamorphic rocks. Bhattacharyya (1971) suggested that metamorphic orthopyroxene has higher $MgO+FeO+Fe_2O_3$ because of replacement of Mg^{2+} by heavier Fe^{2+}, as well as higher Al_2O_3 because of higher pressure conditions. Rietmeijer (1983) broadly confirmed the tendency of metamorphic orthopyroxene to have higher $MgO+FeO+Fe_2O_3$ but considered that Al_2O_3 rather tends to principally reflect the whole-rock chemistry and coexisting or co-precipitating phases. He observed further that metamorphic orthopyroxene has typically low Wo (Deer et al., 1978), and that igneous orthopyroxene may shift into the field of lower-Ca metamorphic orthopyroxene during re-equilibration at high-grade metamorphic conditions. Fewer studies were dedicated to volcanic orthopyroxenes, which were found to contain more significant Fe^{3+} (Ghose and Hafner, 1967; Deer et al., 1978).

Our dataset is largely consistent with such previously acquired knowledge. Colourless and optically positive orthopyroxene shed by ultramafic mantle rocks was confirmed to be the richest by far in Mg and Cr. Orthopyroxene derived from gabbroic rocks re-equilibrated at high-grade metamorphic conditions in the deep structural levels of continental (Ivrea-Verbano) or arc crust (Kohistan), optically distinguished by their pink/green pleochroism, resulted to be poorest in Ca. Volcanic orthopyroxene, optically distinguished by yellow-orange/green pleochroism, resulted to be commonly richer in Fe^{3+}, especially in Kamchatka, Taiwan and Santorini sands but less so in sands derived from the Andean Cordillera or Elbrus and Virunga volcanoes.

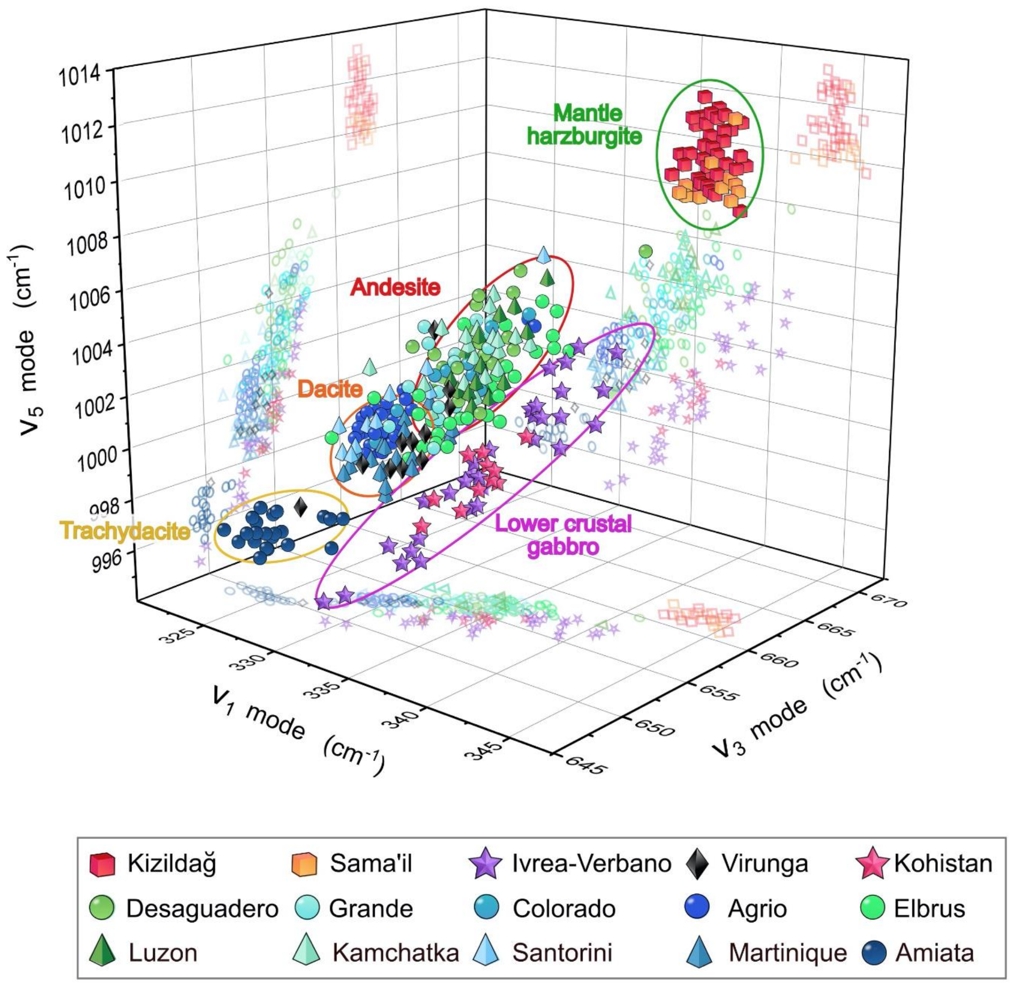

Figure 7. Provenance determination of detrital orthopyroxene with Raman spectroscopy. The 3D plot discriminates OPX composition by using the narrow ν_3 peak (correlating best with Mg#) together with ν_1 (useful to assess Ca content) and the strong ν_5 peak. Colour codes similar as in Fig. 6.

Raman spectroscopy analyses (Fig. 7) allowed us to clearly distinguish among Mg-rich orthopyroxene from mantle harzburgites (ν_1 > 342 cm^{-1}; ν_3 > 661 cm^{-1}; ν_5 > 1009 cm^{-1}), Ca-poor orthopyroxene from gabbroic rocks re-equilibrated at high-temperature conditions in the lower continental or arc crust (high ν_1/ Mg# ratio), and orthopyroxene from mafic to felsic volcanic rocks. Volcanic orthopyroxenes characterized by progressively lower Mg# are distinguished by an up to 20 cm^{-1} shift of all Raman peaks towards lower frequencies. Grains from trachydacites (best fit: ν_1: 322-328; ν_3: 649-652; ν_5: 995-998), dacites (best fit: ν_1: 328-333; ν_3: 653-655; ν_5:999-1003), and andesites (best fit: ν_1: 332-339; ν_3: 653-657; ν_5: 1002-1007) could thus be discriminated (Fig.7). Raman analysis could not distinguish between orthopyroxene from rift-related and arc-related lavas. In summary, optical observations alone are sufficient to discriminate colourless and optically positive enstatite *s.s.* shed by mantle rocks from optically negative pleochroic hypersthene *s.l.*, with the possibility to distinguish further between intrusive/metamorphic and volcanic grains based on their pink/green versus yellow-orange/green pleochroism (Fig. 2). The precise reliable identification of several different provenances, however, requires coupling of optical observations with either chemical or Raman analyses: 1) Mg-rich enstatite *s.s.* from mantle ophiolites; 2) Ca-poor hypersthene *s.l.* from crustal gabbroic rocks; 3) hypersthene *s.l.* from volcanic rocks, with Mg# decreasing from andesites (3A; Mg# 70-65) to dacites (3B; Mg# 60-50), and felsic differentiates (3C; Mg# 50-40). Orthopyroxene derived from rift-related lavas may be characterized by a slightly higher Ca content.

8. Conclusions

Coupling optical observations, SEM-EDS minerochemical analyses, and Raman spectra obtained on 350 orthopyroxene (OPX) grains from 15 modern river and beach sands representing different tectono-stratigraphic levels of continental, arc, and oceanic lithosphere in different geodynamic settings allowed us to distinguish among three main provenances: 1) colourless and optically positive Mg-rich and Cr-rich OPX derived from mantle harzburgites; 2) optically negative Ca-poor OPX showing characteristic pink-reddish/green pleochroism derived from gabbroic rocks re-equilibrated at high temperature conditions in the lower continental crust or arc crust; 3) optically negative OPX showing yellow-orange/green pleochroism derived from volcanic rocks and identified by Mg/(Mg+Fe) atomic ratio decreasing progressively from andesite to dacite and more felsic differentiates. Apart from slightly higher Ca content, OPX from rift-related lavas cannot be distinguished from OPX in volcanic arcs. Chemical data allowed to differentiate among bronzite and hypersthene, which could not be done with optical observations alone.

Accurate information on the chemical composition of detrital orthopyroxene can be very efficiently obtained by Raman spectroscopy, allowing us to build a large and thus more statistically representative database. Although chemical information can be only indirectly obtained, by this simple-to-perform technique we can, in a few seconds and with no additional sample preparation, successfully identify and characterize grains down to the size of a few microns. Changes in En, Fe and Wo in the crystal lattice can be effectively detected by measuring the position of only a few intense Raman vibrational modes.

The present study shows how orthopyroxene contained in mantle rocks exposed in obducted ophiolitic complexes, derived from deep crustal rocks, and shed from volcanic products with different silica content can be most readily distinguished by measuring the positions of the main characteristic Raman peaks (especially ν_1 ~330 cm^{-1}, ν_3 ~655 cm^{-1} or ν_4 ~675 cm^{-1}, and ν_5 ~1002 cm^{-1}). Raman spectroscopy is thus proved to represent a powerful means to efficiently obtain robust high-resolution information in provenance studies.

ACKNOWLEDGMENTS

The studied samples, partly provided by Piero Bellotti, Silvia Bragherio, Giacomo Ghielmi, Filippo Lazzati, Giuditta Radeff and Annalisa Tunesi, were analysed by Giovanni Vezzoli, Alberto Resentini and Ferdinando Moretti Foggia for framework petrography, and by Sergio Andò, Mara Limonta and Marta Padoan for heavy minerals. Mineralogical insights offered by Maria Luce Frezzotti and Rosario Esposito, and technical help by Giovanni Coletti and Guido Pastore are also heartedly acknowledged. The manuscript benefited from careful handling and constructive advice by Editor … and Reviewers …

SUPPLEMENTARY MATERIAL

Supplementary materials associated with this article include information on samples and sampling sites (Table A1), the sand petrography (Table A2) and heavy-mineral datasets (Table A3), the results of Raman spectroscopy analyses carried out at the laboratories of Milano (Table A4) and Parma (Table A5), and the results of SEM-EDS minerochemical analyses (summarized in Table A6 and provided in full in Table A7).

FIGURE CAPTIONS

Figure 2. Comparison between traditional (upper panel; Poldervaart and Hess, 1947) and IMA (lower panel; Morimoto et al., 1988) orthopyroxene classification schemes. En: enstatite; Fs: ferrosilite; Wo: wollastonite.

Figure 2. Typical optical features displayed by orthopyroxene grains derived from mantle, lower crustal, and volcanic rocks. Enstatite *s.s.* from the Kizildağ harzburgite is shown both at parallel and crossed polarizers, whereas other orthopyroxenes are rotated by 90° to show their characteristic pleochroism. Scale bar: 100 μm.

Figure 3. Chemical composition of detrital othopyroxenes determined by SEM-EDS. The 350 analyzed grains from 15 sand samples provide a statistical representation of a range of source-rock lithologies at different structural levels of continental crust, arc crust, and oceanic lithosphere. Only a few grains yielded En values between 85 and 75. En: enstatite; Fs: ferrosilite; Wo: wollastonite. Colour codes similar as in Fig. 6.

Figure 4. Relationships among major chemical elements hosted in detrital orthopyroxenes as determined by SEM-EDS. OPX from mantle harzburgites is highest in Mg, OPX from lower continental and arc crust poorest in Ca. Volcanic OPX, poorer in Al, displays decreasing Mg# from andesite to dacite and more felsic source rocks. Arc and rift-related volcanic OPX are not different. The biplot (Gabriel, 1971) drawn using CoDaPack software by Comas-Cufí and Thió-Henestrosa, 2011) displays multivariate observations (points) and variables (rays). The length of each ray is proportional to the variance of each element in the dataset. If the angle between two rays is close to 0°, 90°, and 180°, then the corresponding compositional parameters are directly correlated, uncorrelated, and inversely correlated, respectively. Colour codes similar as in Fig. 6.

Figure 5. Selected Raman spectra of orthopyroxene grains from diverse source rocks in different geodynamic settings. Baseline subtraction was obtained with Labspec 5 software. Greater background noise for Cr-rich harzburgite-derived OPX is ascribed to Cr-induced fluorescence (Savel'eva et al., 2013). Peaks are stronger for more ordered OPX derived from lower-crustal granulitic metagabbro. In the low-wavelength spectral region, peaks' shape and relative intensity depends on crystal orientation.

Figure 6. Sensitivity of Raman peak positions to Mg# in detrital orthopyroxene as determined by SEM-EDS. The best correlation between peak position and Mg# is obtained for vibrational modes ν3 and ν4, which display excellent linear correlation with each other (middle panel to the right). Among other peaks, ν_1, ν_5, and ν_6 can be used to increase the accuracy of Mg# determination,

whereas ν_2 is least reliable. Colour scale reflects decreasing Mg# from red (Mg# 1.0) to blue (Mg# 0.4).

Figure 7. Provenance determination of detrital orthopyroxene with Raman spectroscopy. The 3D plot discriminates OPX composition by using the narrow ν_3 peak (correlating best with Mg#) together with ν_1 (useful to assess Ca content) and the strong ν_5 peak. Colour codes similar as in Fig. 6.

Table 1. Information on the 15 studied samples of orthopyroxene-rich river and beach sands exclusively or dominantly derived from a range of mantle, deep-crustal, and volcanic rocks generated in different geodynamic settings.

Table 2. Chemical composition of detrital othopyroxenes analyzed by SEM-EDS. Note high Si and Cr in Mg-rich OPX from mantle rocks and low Ca in OPX from lower-crustal Ivrea-Verbano metagabbros and Kohistan arc intrusives; all these OPX are Ti-poor. Fe-rich OPX from Mt. Amiata is poor in Si and Al. No distinctive features are displayed by OPX from Virunga trachytes. Mg#: Mg/(Mg+Fe) atomic ratio; En: enstatite; Fs: ferrosilite; Wo: wollastonite; b.d.l.: below detection limit.

Table 3. Mean, minimum and maximum Raman peak positions (vibrational modes ν1 to ν6) distinctive of detrital othopyroxene derived from a range of mantle, deep crustal, and volcanic rocks representing different geodynamic settings. Mg#: Mg/(Mg+Fe) atomic ratio.

Table 4. Mg# calculated from Raman peak positions. R^2 and σMg# represent the proportion of the variation and expected uncertainty when Mg# is derived from the value of a single Raman peak.

CITED REFERENCES

Agostini, S., Doglioni, C., Innocenti, F., Manetti, P. and Tonarini, S. (2010) On the geodynamics of the Aegean rift. *Tectonophysics*, **488**(1-4), 7-21.

Andersen, T., Kristoffersen, M. and Elburg, M.A. (2016) How far can we trust provenance and crustal evolution information from detrital zircons? A South African case study. *Gondwana Research*, **34**,129-148.

Andò, S. (2020) Gravimetric separation of heavy minerals in sediments and rocks. *Minerals*, **10**(3), 273.

Andò, S. and Garzanti, E. (2014). Raman spectroscopy in heavy-mineral studies. In *Geological Society*, London, Special Publications, **386**(1), 395-412.

Aoki, K. I., Yoshida, T. and Jin, Y. Z. (1989) Petrology and geochemistry of Pleistocene dacitic and rhyolitic pyroclastic flows from southern part of northeast Honshu, Japan. *Journal of mineralogy, petrology and economic geology*, **84**(1), 1-14.

Basu, A. (2017) Evolution of siliciclastic provenance inquiries: A critical appraisal. In: *Sediment Provenance, Influences on Compositional Change from Source to Sink. 2* (eds. Mazumder, R.). Elsevier, pp. 5–23.

Bhattacharyya, C. (1971) An evaluation of the chemical distinctions between igneous and metamorphic orthopyroxenes. *American Mineralogist: Journal of Earth and Planetary Materials*, **56**(3-4 Part 1), 499-506.

Bersani, D., Andò, S., Vignola, P., Moltifiori, G., Marino, I. G., Lottici, P. P. and Diella, V. (2009) Micro-Raman spectroscopy as a routine tool for garnet analysis. *Spectrochimica Acta Part A: Molecular and Biomolecular Spectroscopy*, **73**(3), 484-491.

Bersani, D., Aliatis, I., Tribaudino, M., Mantovani, L., Benisek, A., Carpenter, M. A., Gatta, G. D. and Lottici, P. P. (2018) Plagioclase composition by Raman spectroscopy. *Journal of Raman Spectroscopy*, **49**(4), 684-698.

Borromeo, L., Zimmermann, U., Andò, S., Coletti, G., Bersani, D., Basso, D., Gentile, P., Schulz, B. and Garzanti, E. (2017) Raman spectroscopy as a tool for magnesium estimation in Mg-calcite. *Journal of Raman Spectroscopy*, **48**(7), 983-992.

Borromeo, L., Egeland, N., Wetrhus Minde, M., Zimmermann, U., Andò, S., Madland, M. V. and Korsnes, R. I. (2018) Quick, easy, and economic mineralogical studies of flooded chalk for EOR experiments using Raman spectroscopy. *Minerals*, **8**(6), 221.

Bouysse, P., Westercamp, D. and Andreieff, P. (1990) The Lesser Antilles Island Arc. In *Proceedings of the Ocean Drilling Program, Scientific Results (eds.* Moore, J.C, Mascle, A., et al.) **110**,4, 29-44.

Bowen, N.L. (1935) Ferrosilite as a natural mineral. *American Journal of Science*, **5**(30), 481.

Burns, R. G. (1966) Origin of optical pleochroism in orthopyroxenes. *Mineralogical magazine and journal of the Mineralogical Society*, **35**(273), 715-719.

Byrne, T., Chan, Y.C., Rau, R.J., Lu, C.Y., Lee, Y.H. and Wang, Y.J. (2011) The arc–continent collision in Taiwan. In *Arc-continent collision*. Springer, Berlin, Heidelberg. pp. 213-245.

Cameron, M. and Papike, J. J. (1981) Structural and chemical variations in pyroxenes. *American Mineralogist*, **66**(1-2), 1-50.

Caracciolo, L. (2020) Sediment generation and sediment routing systems from a quantitative provenance analysis perspective: Review, application and future development. *Earth-Science Reviews*, **209**, 103226.

Caracciolo, L., Orlando, A., Marchev, P., Critelli, S., Manetti, P., Raycheva, R. and Riley, D. (2016) Provenance of Tertiary volcanoclastic sediment in NW Thrace (Bulgaria): Evidence from detrital amphibole and pyroxene geochemistry. *Sedimentary Geology*, **336**, 120-137.

Cawood, P.A. (1983) Modal composition and detrital clinopyroxene geochemistry of lithic sandstones from the New England Fold Belt (east Australia): A Paleozoic forearc terrane.

Geological Society of America Bulletin, **94**(10), 1199-1214.

Colombo, A. and Tunesi, A. (1999) Alpine metamorphism of the Southern Alps west of the Giudicarie Line. *Schweizerische Mineralogische und Petrographische Mitteilungen*, **79**(1), 183-189.

Comas-Cufí, M. and Thió-Henestrosa, F.S. (2011) CoDaPack 2.0: A Stand-Alone, Multi-Platform Compositional Software. In *Proceedings of the 4th International Workshop on Compositional Data Analysis*, Girona, Spain, 10–13.

Deer, W. A., Howie, R. A., & Zussman, J. (1997) *Rock-forming minerals: single-chain silicates, Volume 2A.* Geological Society of London, London, pp.992.

Delmonte, B., Paleari, C. I., Andò, S., Garzanti, E., Andersson, P. S., Petit, J. R., Crosta, X., Narcisi, B., Baroni, C., Salvatore, M. C., Baccolo, G. and Maggi, V. (2017) Causes of dust size variability in central East Antarctica (Dome B): Atmospheric transport from expanded South American sources during Marine Isotope Stage 2. *Quaternary Science Reviews*, **168**, 55-68.

Deruelle, B. (1982) Petrology of the Plio-Quaternary volcanism of the south-central and meridional Andes. *Journal of Volcanology and Geothermal Research*, **14**(1-2), pp.77-124.

Dilek, Y. and Thy, P. (1998) Structure, petrology and seafloor spreading tectonics of the Kizildag ophiolite, Turkey. *Geological Society*, Special Publications, London, **148**(1), pp.43-69.

Dilek, Y. and Newcomb, S. (2003) Ophiolite concept and its evolution. *Special Papers-Geological Society of America*, 1-16.

Druitt, T.H., Edwards, L., Mellors, R.M., Pyle, D.M., Sparks, R.S.J., Lanphere, M., Davies, M. and Barreirio, B. (1999) Santorini Volcano (with a Geological map of the Santorini islands, Scale 1/20.000). *Geological Society of London*, Memoir, **19**, 165.

Dunkl, I., von Eynatten, H., Andò, S., Lünsdorf, K., Morton, A., Alexander, B., ... & Yoshida, K. (2020) Comparability of heavy mineral data–The first interlaboratory round robin test. *Earth-Science Reviews*, **211**, 103210.

Dupuy, C., Dostal, J., Traineau, H. (1985) Geochemistry of volcanic rocks from Mt. Pelée, Martinique. *Journal of volcanology and geothermal research*, **26**(1-2), 147-165.

Ebinger, C., and Furman, T. (2003) Geodynamical setting of the Virunga volcanic province, East Africa. *Acta Vulcanologica*, **14**(1/2), 9.

Eggler, D. H. (1986) Kimberlites: how do they form?. In *International Kimberlite Conference: Extended Abstracts*, **4**, 155-159.

Ferrari, L., Conticelli, S., Burlamacchi, L. and Manetti, P. (1996) Volcanological evolution of the Monte Amiata, Southern Tuscany: new geological and petrochemical data. *Acta Vulcanologica*, **8**, 41-56.

Frezzotti, M. L., Tecce, F., and Casagli, A. (2012) Raman spectroscopy for fluid inclusion analysis. *Journal of Geochemical Exploration*, **112**, 1-20.

Francalanci, L., Vougioukalakis, G. E., Perini, G., and Manetti, P. (2005) A West-East Traverse along the magmatism of the south Aegean volcanic arc in the light of volcanological, chemical and isotope data. In *Developments in Volcanology*, 7, Elsevier. pp. 65-111.

Gabriel, K.R. (1971) The biplot graphic display of matrices with application to principal component analysis. *Biometrika*, **58**, 453–467.

Garzanti, E. (2016) From static to dynamic provenance analysis—Sedimentary petrology upgraded. *Sedimentary Geology*, **336**, 3-13.

Garzanti, E. (2019) Petrographic classification of sand and sandstone. *Earth-Science Reviews*, **192**, 545-563.

Garzanti, E. and Andò, S. (2007) Plate tectonics and heavy mineral suites of modern sands. In *Heavy Minerals in Use* (eds. Mange, M. and Wright, D). Elsevier, Amsterdam, Developments in Sedimentology, **58**, 741-763.

Garzanti, E. and Andò, S. (2019) Heavy minerals for junior woodchucks. *Minerals*, **9**(3), 148.

Garzanti, E. and Resentini, A. (2016). Provenance control on chemical indices of weathering (Taiwan river sands). *Sedimentary Geology*, **336**, 81-95.

Garzanti, E., Ando, S. and Scutella, M. (2000) Actualistic ophiolite provenance: the Cyprus case. *The Journal of Geology*, **108**(2), 199-218.

Garzanti, E., Vezzoli, G. and Ando, S. (2002a) Modern sand from obducted ophiolite belts (Sultanate of Oman and United Arab Emirates). *The Journal of geology*, **110**(4), 371-391.

Garzanti, E., Canclini, S., Moretti Foggia, F. and Petrella, N. (2002b) Unraveling magmatic and orogenic provenance in modern sand: the back-arc side of the Apennine thrust belt, Italy. *Journal of Sedimentary Research*, **72**(1), 2-17.

Garzanti, E., Vezzoli, G., Andò, S., Paparella, P. and Clift, P.D. (2005) Petrology of Indus River sands: a key to interpret erosion history of the Western Himalayan Syntaxis. *Earth and Planetary Science Letters*, **229**(3-4), 287-302.

Garzanti, E., Ando, S. and Vezzoli, G. (2006) The continental crust as a source of sand (southern Alps cross section, northern Italy). *The Journal of Geology*, **114**(5), 533-554.

Garzanti, E., Padoan, M., Andò, S., Resentini, A., Vezzoli, G. and Lustrino, M. (2013) Weathering and relative durability of detrital minerals in equatorial climate: sand petrology and geochemistry in the East African Rift. *The Journal of Geology*, **121**(6), 547-580.

Garzanti, E., Andò, S., Limonta, M., Fielding, L., Najman, Y. (2018) Diagenetic control on mineralogical suites in sand, silt, and mud (Cenozoic Nile Delta): Implications for provenance reconstructions. *Earth-Science Reviews*, **185**, 122-139.

Garzanti, E., Capaldi, T., Vezzoli, G., Limonta, M. and Sosa, N. (2021a) Transcontinental retroarc sediment routing controlled by subduction geometry and climate change (Central and Southern Andes, Argentina). *Basin Research*. **33**(6), 3406-3437.

Garzanti, E., Limonta, M., Vezzoli, G. and Sosa, N. (2021b) From Patagonia to Río de la Plata: Multistep long-distance littoral transport of Andean volcaniclastic sand along the Argentine passive margin. *Sedimentology*, **68**, 3357–3384.

Gehrels, G. (2011) Detrital zircon U-Pb geochronology: Current methods and new opportunities. In: Busby, C., and Azor, A., *Tectonics of Sedimentary Basins: Recent Advances*. Blackwell, Oxford. pp. 47-62.

Germa, A., Quidelleur, X., Lahitte, P., Labanieh, S. and Chauvel, C. (2011) The K–Ar Cassignol–Gillot technique applied to western Martinique lavas: a record of Lesser Antilles arc activity from 2 Ma to Mount Pelée volcanism. *Quaternary Geochronology*, **6**(3-4), 341-355.

Ghose, S., and Hafner, S. (1967) Mg^{2+}–Fe^{2+} distribution in metamorphic and volcanic orthopyroxenes. *Zeitschrift für Kristallographie-Crystalline Materials*, **125**(1-6), 157-162.

Greensfelder, L. (2002) Subtleties of sand reveal how mountains crumble. *Science*, **295**(5553). pp. 256-258.

Griffith, W. P. (1969) Raman studies on rock-forming minerals. Part I. Orthosilicates and cyclosilicates. *Journal of the Chemical Society A: Inorganic, Physical, Theoretical*, 1372-1377.

Guo, R., Hu, X., Garzanti, E., Lai, W., Yan, B. and Mark, C. (2020) How faithfully do the geochronological and geochemical signatures of detrital zircon, titanite, rutile and monazite record magmatic and metamorphic events? A case study from the Himalaya and Tibet. *Earth-Science Reviews*, **201**, 103082.

Guo, R., Hu, X., Garzanti, E. and Lai, W. (2021) Boron isotope composition of detrital tourmaline: A new tool in provenance analysis. *Lithos*, **400**, 106360.

Heymann, D. (1967) On the origin of hypersthene chondrites: Ages and shock effects of black chondrites. *Icarus*, **6**(1-3), 189-221.

Hope, G. A., Woods, R. and Munce, C. G. (2001) Raman microprobe mineral identification. *Minerals Engineering*, **14**(12), 1565-1577.

Howie, R. A., and Smith, J. V. (1966) X-Ray-Emission Microanalysis of Rock-Forming Minerals. V. Orthopyroxenes. *The Journal of Geology*, **74**(4), 443-462.

Hu, X., An, W., Wang, J., Garzanti, E. and Guo, R. (2014) Himalayan detrital chromian spinels and timing of Indus-Yarlung ophiolite erosion. *Tectonophysics*, **621**, 60-68.

Huang, E., Chen, C. H., Huang, T., Lin, E. H. and Xu, J. A. (2000) Raman spectroscopic characteristics of Mg-Fe-Ca pyroxenes. *American Mineralogist*, **85**(3-4), 473-479.

Ingersoll, R.V., Bullard, T.F., Ford, R.L., Grimm, J.P., Pickle, J.D. and Sares, S.W. (1984) The effect of grain size on detrital modes: a test of the Gazzi-Dickinson point-counting method. *Journal of Sedimentary Petrology*, **54**(1), 103-116.

Jagoutz, O. and Schmidt, M.W. (2012) The formation and bulk composition of modern juvenile continental crust: The Kohistan arc. *Chemical Geology*, **298**, 79-96.

Jan, M. Q., & Howie, R. A. (1980) Ortho-and clinopyroxenes from the pyroxene granulites of Swat Kohistan, northern Pakistan. *Mineralogical Magazine*, **43**(330), 715-726.

Kay, S.M., Godoy, E. and Kurtz, A. (2005) Episodic arc migration, crustal thickening, subduction erosion, and magmatism in the south-central Andes. *Geological Society of America Bulletin*, **117**(1-2), 67-88.

Kleiman, L.E. and Japas, M.S. (2009) The Choiyoi volcanic province at 34°S–36°S (San Rafael, Mendoza, Argentina): Implications for the Late Palaeozoic evolution of the southwestern margin of Gondwana. *Tectonophysics*, **473**(3-4), 283-299.

Kubovics, I., Ditrói Puskás, Z., and Gál-Sólymos, K. (2004). Re-evaluation of meteorites from the Carpathian Basin: Preliminary results from Kisvarsány, Knyahinya, Mezőmadaras, Mike, Mócs and Nyírábrány. *Acta Geologica Hungarica*, **47**(2-3), 269-285.

Gismelseed, A. M., Bashir, S., Worthing, M. A., Yousif, A. A., Elzain, M. E., Rawas, A. A., and Widatallah, H. M. (2005). Studies and characterizations of the Al Zarnkh meteorite. *Meteoritics & Planetary Science*, **40**(2), 255-259.

Kuebler, K., Wang, A., Freeman, J. J. and Jolliff, B. L. (2006). Database of Raman mineral spectra for planetary surface exploration. In *37th Annual Lunar and Planetary Science Conference*, pp.1907.

Kuno, H. (1954). Study of orthopyroxenes from volcanic rocks. *American Mineralogist: Journal of Earth and Planetary Materials*, **39**(1-2), 30-46.

Lai, Y.M., Song, S.R., Lo, C.H., Lin, T.H., Chu, M.F. and Chung, S.L. (2017) Age, geochemical and isotopic variations in volcanic rocks from the Coastal Range of Taiwan: Implications for magma generation in the Northern Luzon Arc. *Lithos*, **272**, 92-115.

Lebedev, V.A., Chernyshev, I.V., Chugaev, A.V., Gol'tsman, Y.V. and Bairova, E.D. (2010) Geochronology of eruptions and parental magma sources of Elbrus volcano, the Greater Caucasus: K-Ar and Sr-Nd-Pb isotope data. *Geochemistry International*, **48**(1), 41-67.

Lee, J.I., Clift, P.D., Layne, G., Blum, J. and Khan, A.A. (2003) Sediment flux in the modern Indus River inferred from the trace element composition of detrital amphibole grains. *Sedimentary Geology*, **160**(1-3), 243-257.

Leslie, A. G., & Nutman, A. P. (2003). Evidence for Neoproterozoic orogenesis and early high temperature Scandian deformation events in the southern East Greenland Caledonides. *Geological Magazine*, **140**(3), 309-333.

Liang, W., Garzanti, E., Andò, S., Gentile, P. and Resentini, A. (2019) Multimineral fingerprinting of Transhimalayan and Himalayan sources of Indus-derived Thal Desert sand (central Pakistan). *Minerals*, **9**(8), 457.

Limonta, M., Garzanti, E., Resentini, A., Andò, S., Boni, M. and Bechstädt, T. (2015) Multicyclic sediment transfer along and across convergent plate boundaries (Barbados, Lesser Antilles). *Basin Research*, **27**(6), 696-713.

Lindh, A. (1975) Coexisting pyroxenes—a multivariate statistical approach. *Lithos*, **8**(2), 151-161.

Lindsley, D. H. (1965) Ferrosilite. *Carnegie Institution Washington Yearbook*, **64**, 148-150.

Lippard, S.J. (1986) The ophiolite of northern Oman. *Geological Society London Memoir*, **11**,178.

Lorenz, C. A., Ivanova, M. A., Brandstaetter, F., Kononkova, N. N., and Zinovieva, N. G. (2020). Aubrite Pesyanoe: Clues to composition and evolution of the enstatite achondrite parent body. *Meteoritics & Planetary Science*, **55**(12), 2670-2702.

Makreski, P., Jovanovski, G., Gajović, A., Biljan, T., Angelovski, D. and Jaćimović, R. (2006) Minerals from Macedonia. XVI. Vibrational spectra of some common appearing pyroxenes and pyroxenoids. *Journal of Molecular Structure*, **788**(1-3), 102-114.

Mange, M.A. and Maurer, H.F.W. (1992) Heavy Minerals in Colour. Chapman & Hall, London, **147**.

Mange, M.A. and Morton, A.C. (2007) Geochemistry of heavy minerals In Mange, M. & Wright, D. (eds.), Heavy Minerals in Use. Elsevier, Amsterdam, *Developments in Sedimentology*, **58**, 345-391.

Marinos, V., Prountzopoulos, G., Asteriou, P., Papathanassiou, G., Kaklis, T., Pantazis, G., Lambrou, E., Grendas, N., Karantanellis, E. and Pavlides, S. (2017) Beyond the boundaries of feasible engineering geological solutions: stability considerations of the spectacular Red Beach cliffs on Santorini Island, Greece. *Environmental Earth Sciences*, **76**(15), 1-14.

Mason, B. (1966) The enstatite chondrites. *Geochimica et Cosmochimica Acta*, **30**(1), 23-39.

Meinhold, G. (2010) Rutile and its applications in earth sciences. *Earth-Science Reviews*, **102**(1-2), 1-28.

Mernagh, T. P. and Hoatson, D. M. (1997) Raman spectroscopic study of pyroxene structures from the Munni Munni layered intrusion, Western Australia. *Journal of Raman Spectroscopy*, **28**(9), 647-658.

Morimoto, N. (1988) Nomenclature of pyroxenes. *Mineralogy and Petrology*, **39**(1), 55-76.

Morse, S. A. (1975) Plagioclase lamellae in hypersthene, Tikkoatokhakh Bay, Labrador. *Earth and Planetary Science Letters*, **26**(3), 331-336.

Morton, A.C. and Hallsworth, C. (2007) Stability of detrital heavy minerals during burial diagenesis. In *Heavy Minerals in Use* (eds. Mange, M. and Wright, D.). Elsevier, Amsterdam, *Developments in Sedimentology*, **58**. pp. 215-245.

O'Sullivan, G., Chew, D., Kenny, G., Henrichs, I. and Mulligan, D. (2020) The trace element composition of apatite and its application to detrital provenance studies. *Earth-Science Reviews*, **201**, 103044.

Papike, J. J., Fowler, G. W., Shearer, C. K. and Layne, G. D. (1996) Ion microprobe investigation of plagioclase and orthopyroxene from lunar Mg-suite norites: implications for calculating parental melt REE concentrations and for assessing postcrystallization REE redistribution. *Geochimica et Cosmochimica Acta*, **60**(20), 3967-3978.

Pastore, G., Baird, T., Vermeesch, P., Resentini, A. and Garzanti, E. (2021) Provenance and recycling of Sahara Desert sand. *Earth-Science Reviews*, 103606.

Poldervaart, A. (1947) The relationship of orthopyroxene to pigeonite. *Mineralogical Magazine and Journal of the Mineralogical Society*, **28**(198), 164-172.

Pouclet, A., Bellon, H. and Bram, K. (2016) The Cenozoic volcanism in the Kivu rift: Assessment of the tectonic setting, geochemistry, and geochronology of the volcanic activity in the South-Kivu and Virunga regions. *Journal of African Earth Sciences*, **121**, 219-246.

Quick, J.E., Sinigoi, S. and Mayer, A. (1994) Emplacement dynamics of a large mafic intrusion in the lower crust, Ivrea-Verbano Zone, northern Italy. *Journal of Geophysical Research: Solid Earth*, **99**(B11), 21559-21573.

Raman, C. V. (1928) A change of wave-length in light scattering. *Nature*, **121**(3051), 619-619.

Ramos, V.A. and Folguera, A. (2011) Payenia volcanic province in the Southern Andes: An appraisal of an exceptional Quaternary tectonic setting. *Journal of Volcanology and geothermal Research*, **201**(1-4), 53-64.

Ramos, V.A. and Kay, S.M. (2006) Overview of the tectonic evolution of the southern Central Andes of Mendoza and Neuquén (35°–39°S latitude). In *Evolution of an Andean margin: A tectonic and magmatic view from the Andes to the Neuquén Basin (35°–39°S latitude)* (eds. Kay, S.M., and Ramos, V.A.). Geological Society of America Special Paper 407. pp. 1–17.

Ramos, V.A., Cristallini, E.O. and Pérez, D.J. (2002) The Pampean flat-slab of the Central Andes. *Journal of South American Earth Sciences*, **15**(1), 59-78.

Rezvukhin, D. I., Alifirova, T. A., Korsakov, A. V. and Golovin, A. V. (2019). A new occurrence of yimengite-hawthorneite and crichtonite-group minerals in an orthopyroxenite from kimberlite: Implications for mantle metasomatism. *American Mineralogist: Journal of Earth and Planetary Materials*, **104**(5), 761-774.

Rietmeijer, F. J. (1983) Chemical distinction between igneous and metamorphic orthopyroxenes especially those coexisting with Ca-rich clinopyroxenes: a re-evaluation. *Mineralogical Magazine*, **47**(343), 143-151.

Rivalenti, G., Garuti, G., Rossi, A., Siena, F. and Sinigoi, S. (1981) Existence of different peridotite types and of a layered igneous complex in the Ivrea Zone of the Western Alps. *Journal of Petrology*, **22**(1), 127-153.

Rogers, N.W., James, D., Kelley, S.P. and De Mulder, M. (1998) The generation of potassic lavas from the eastern Virunga province, Rwanda. *Journal of Petrology*, **39**(6), 1223-1247.

Savel'eva, G. N., Batanova, V. G., Sobolev, A. V., and Kuz'min, D. V. (2013). Minerals of mantle peridotites: Indicators of chromium ores in ophiolites. In *Doklady Earth Sciences*, Springer Nature BV, **452** (1), p. 963).

Searle, M. and Cox, J. (1999) Tectonic setting, origin, and obduction of the Oman ophiolite. *Geological Society of America Bulletin*, **111**(1), 104-122.

Searle, M.P., Khan, M.A., Fraser, J.E., Gough, S.J. and Jan, M.Q. (1999) The tectonic evolution of the Kohistan-Karakoram collision belt along the Karakoram Highway transect, north Pakistan. *Tectonics*, **18**(6), 929-949.

Serri, G., Innocenti, F. and Manetti, P. (1993) Geochemical and petrological evidence of the subduction of delaminated Adriatic continental lithosphere in the genesis of the Neogene-Quaternary magmatism of central Italy. *Tectonophysics*, **223**(1-2), 117-147.

Skridlaitė, G., Šiliauskas, L., Prušinskienė, S., & Bagiński, B. (2019). Petrography and mineral chemistry of the Varena Iron Ore deposit, southeastern Lithuania: implications for the evolution of carbonate and silicate rocks and ore mineralization. *Baltica*, **32**(1), 107-126.

Stalder, R., Kronz, A. and Schmidt, B. C. (2009) Raman spectroscopy of synthetic (Mg, Fe) SiO_3 single crystals. An analytical tool for natural orthopyroxenes. *European Journal of Mineralogy*, **21**(1), 27-32.

Stangarone, C., Tribaudino, M., Prencipe, M. and Lottici, P. P. (2016) Raman modes in Pbca enstatite ($Mg_2Si_2O_6$): an assignment by quantum mechanical calculation to interpret experimental results. *Journal of Raman Spectroscopy*, **47**(10), 1247-1258.

Stangarone, C., Maturilli, A., & Helbert, J. (2021, March). Calculated High Temperature Thermal-IR Spectra of Orthoenstatite: Theoretical Insights on Band Shifts and Temperature. In *Lunar and Planetary Science Conference* (No. 2548, p. 2079).

Stolper, E., and McSween Jr, H. Y. (1979) Petrology and origin of the shergottite meteorites. *Geochimica et Cosmochimica Acta*, **43**(9), 1475-1498.

Sturm, R. (2002). PX-NOM—an interactive spreadsheet program for the computation of pyroxene analyses derived from the electron microprobe. *Computers & Geosciences*, **28**(4), 473-483.

Suggate, S.M. and Hall, R. (2014) Using detrital garnet compositions to determine provenance: a new compositional database and procedure. *Special Publications,* Geological Society, London, **386**(1), 373-393.

Tribaudino, M., Mantovani, L., Bersani, D. and Lottici, P. P. (2011) Raman investigation on pigeonite in ureilite. *Spectroscopy Letters*, **44**(7-8), 480-485.

Tribaudino, M., Mantovani, L., Bersani, D. and Lottici, P. P. (2012). Raman spectroscopy of (Ca, Mg) $MgSi_2O_6$ clinopyroxenes. *American Mineralogist*, **97**(8-9), 1339-1347.

Tribaudino, M., Aliatis, I., Bersani, D., Gatta, G. D., Lambruschi, E., Mantovani, L., ... and Lottici, P. P. (2017) High-pressure Raman spectroscopy of Ca (Mg, Co) Si_2O_6 and Ca (Mg, Co) Ge_2O_6 clinopyroxenes. *Journal of Raman Spectroscopy*, **48**(11), 1443-1448.

Tribaudino, M., Stangarone, C., Gori, C., Mantovani, L., Bersani, D., and Lottici, P. P. (2019). Experimental and calculated Raman spectra in Ca–Zn pyroxenes and a comparison between ($Ca_xM^{2+}{}_{1-x}$) $M^{2+}Si_2O_6$ pyroxenes (M^{2+}= Mg, Co, Zn, Fe^{2+}). *Physics and Chemistry of Minerals*, **46**(9), 827-837.

Vezzoli, G., Garzanti, E., Limonta, M. and Radeff, G. (2020) Focused erosion at the core of the Greater Caucasus: Sediment generation and dispersal from Mt. Elbrus to the Caspian Sea. *Earth-Science Reviews*, **200**, 102987.

Viccaro, M., Giuffrida, M., Nicotra, E. and Ozerov, A.Y. (2012) Magma storage, ascent and recharge history prior to the 1991 eruption at Avachinsky Volcano, Kamchatka, Russia: Inferences on the plumbing system geometry. *Lithos*, **140**, 11-24.

Vincent, S.J., Somin, M.L., Carter, A., Vezzoli, G., Fox, M. and Vautravers, B. (2020) Testing models of Cenozoic exhumation in the Western Greater Caucasus. *Tectonics*, **39**(2).

Volynets, A. O., Churikova, T. G., Wörner, G., Gordeychik, B. N. and Layer, P. (2010) Mafic Late Miocene–Quaternary volcanic rocks in the Kamchatka back arc region: implications for subduction geometry and slab history at the Pacific–Aleutian junction. *Contributions to mineralogy and petrology*, **159**(5), 659-687.

von Eynatten, H. and Dunkl, I. (2012) Assessing the sediment factory: the role of single grain analysis. *Earth-Science Reviews*, **115**(1-2), 97-120.

Wang, A., Jolliff, B. L., Haskin, L. A., Kuebler, K. E. and Viskupic, K. M. (2001) Characterization and comparison of structural and compositional features of planetary quadrilateral pyroxenes by Raman spectroscopy. *American Mineralogist*, **86**(7-8), 790-806.

White, W. B. (1975) Structural interpretation of lunar and terrestrial minerals by Raman spectroscopy. *Infrared and Raman spectroscopy of Lunar and terrestrial minerals*, 325-358.

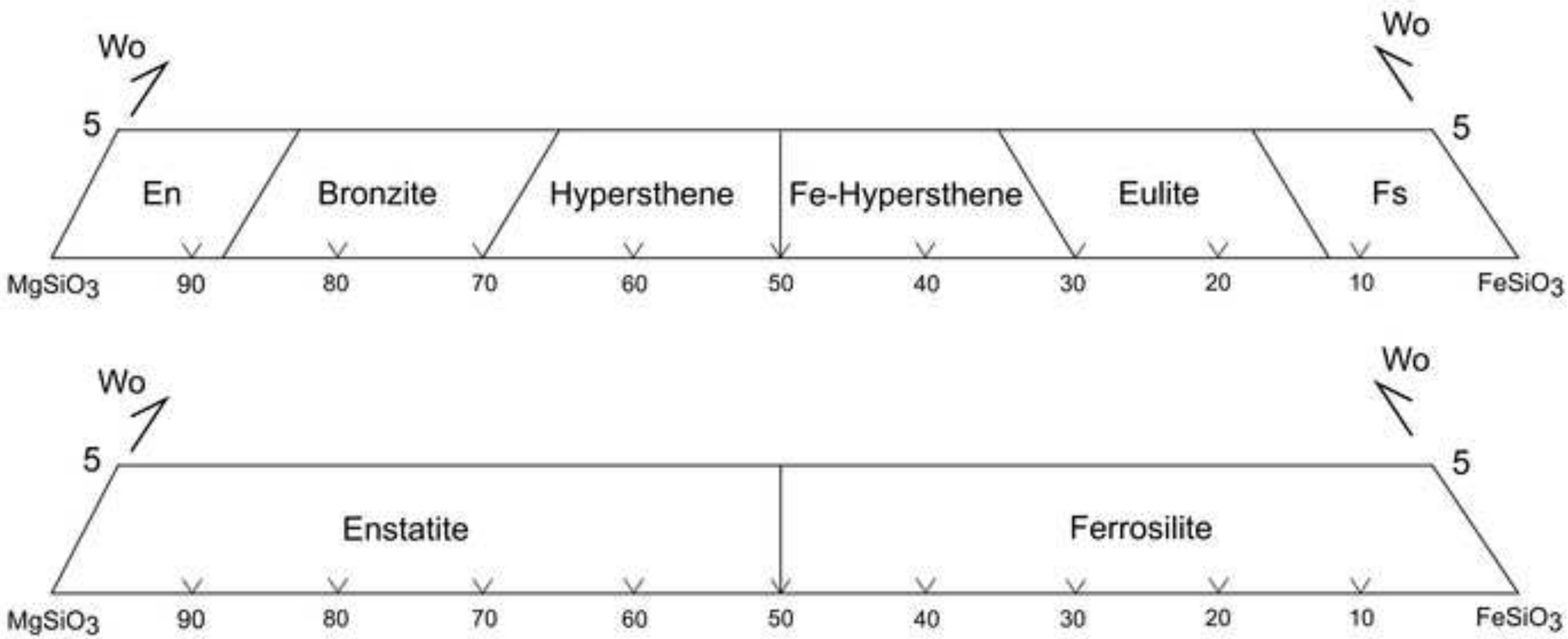
Wo
Wo
5
5
En
Bronzite
Hypersthene
Fe-Hypersthene
Eulite
Fs
$MgSiO_3$
90
80
70
60
50
40
30
20
10
$FeSiO_3$
Wo
Wo
5
5
Enstatite
Ferrosilite
$MgSiO_3$
90
80
70
60
50
40
30
20
10
$FeSiO_3$

Click here to access/download;Figure;Figure 2 Borromeo.jpg

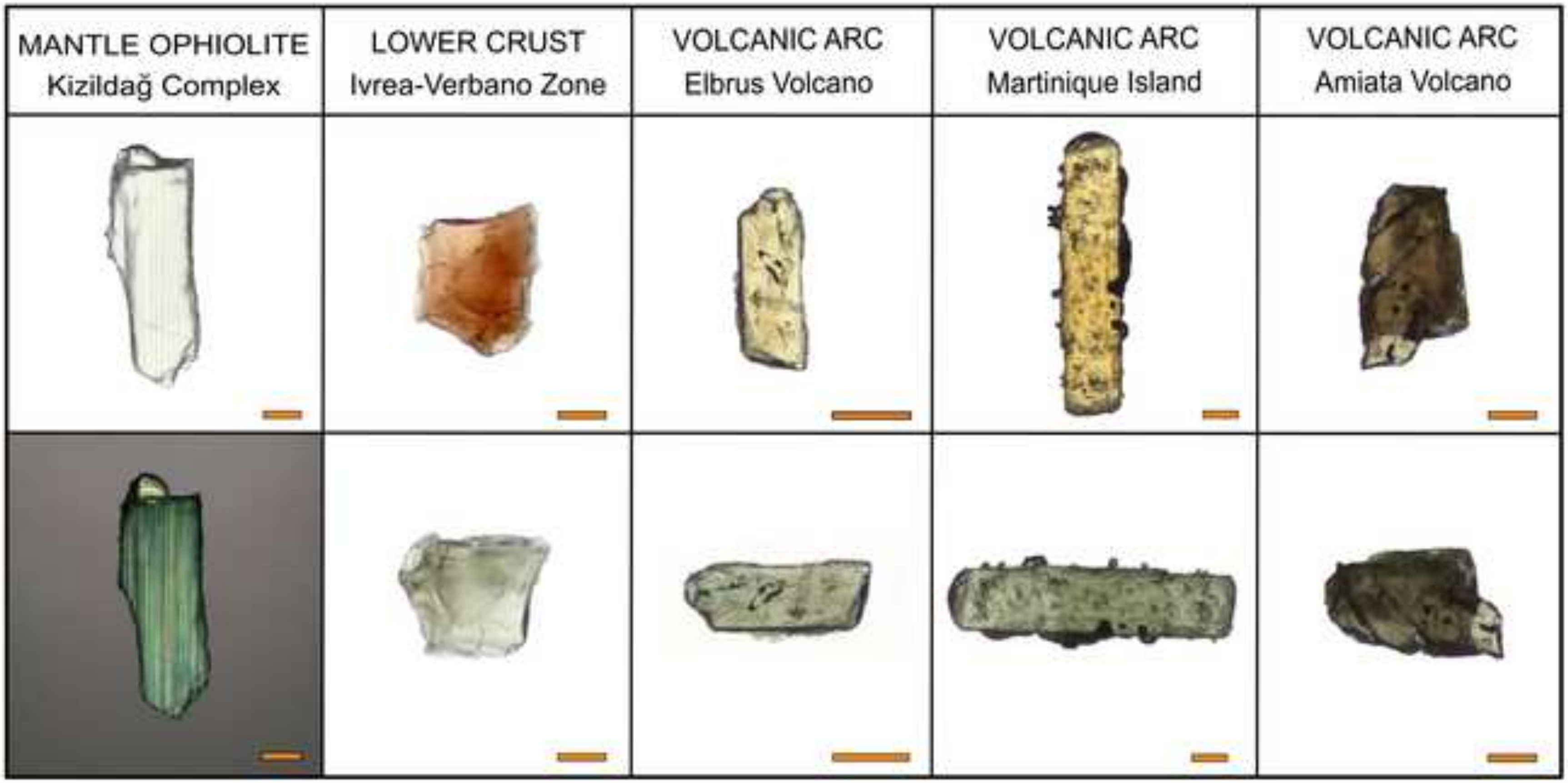

Click here to access/download;Figure;Figure 3 Borromeo.jpg

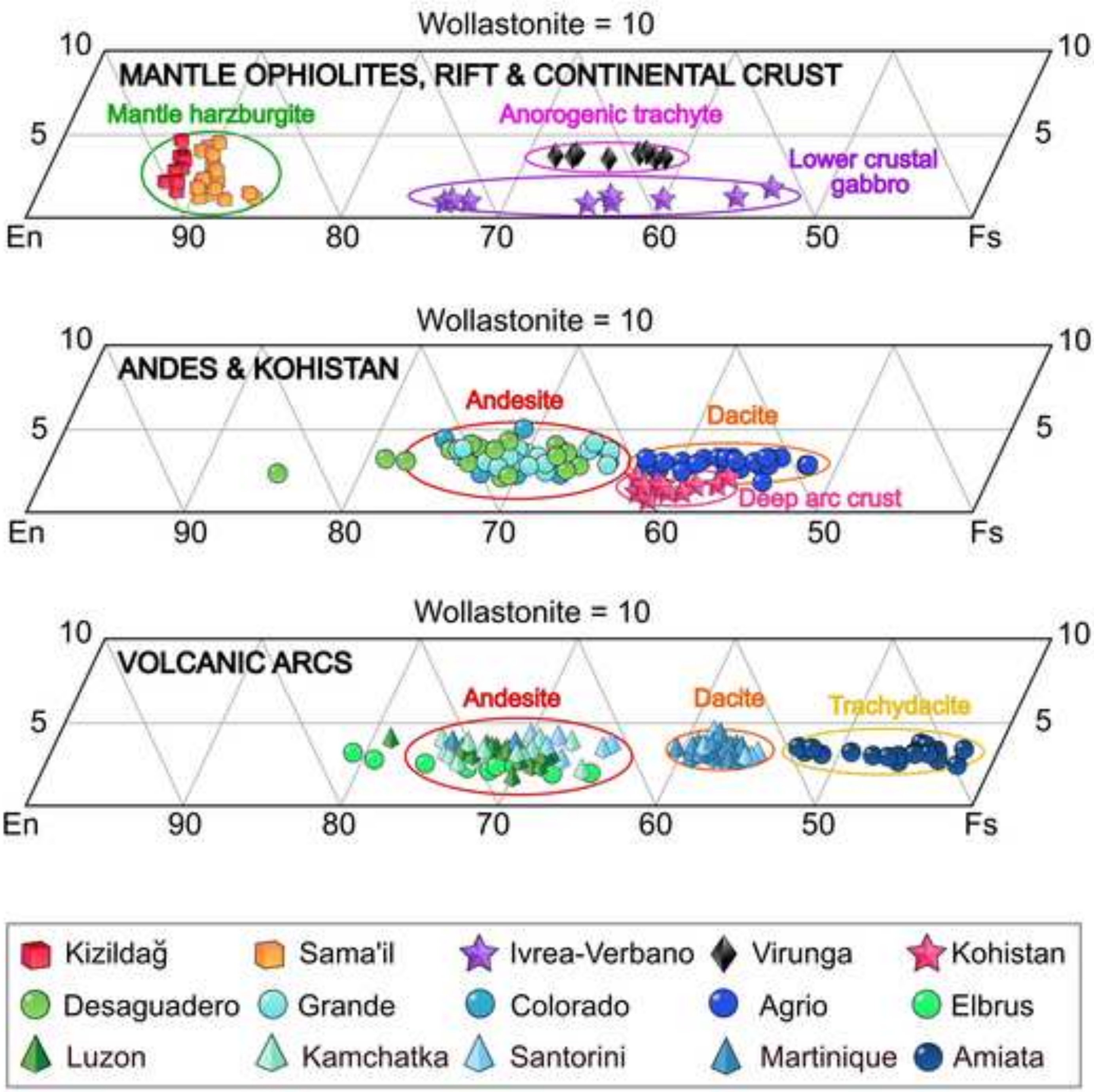

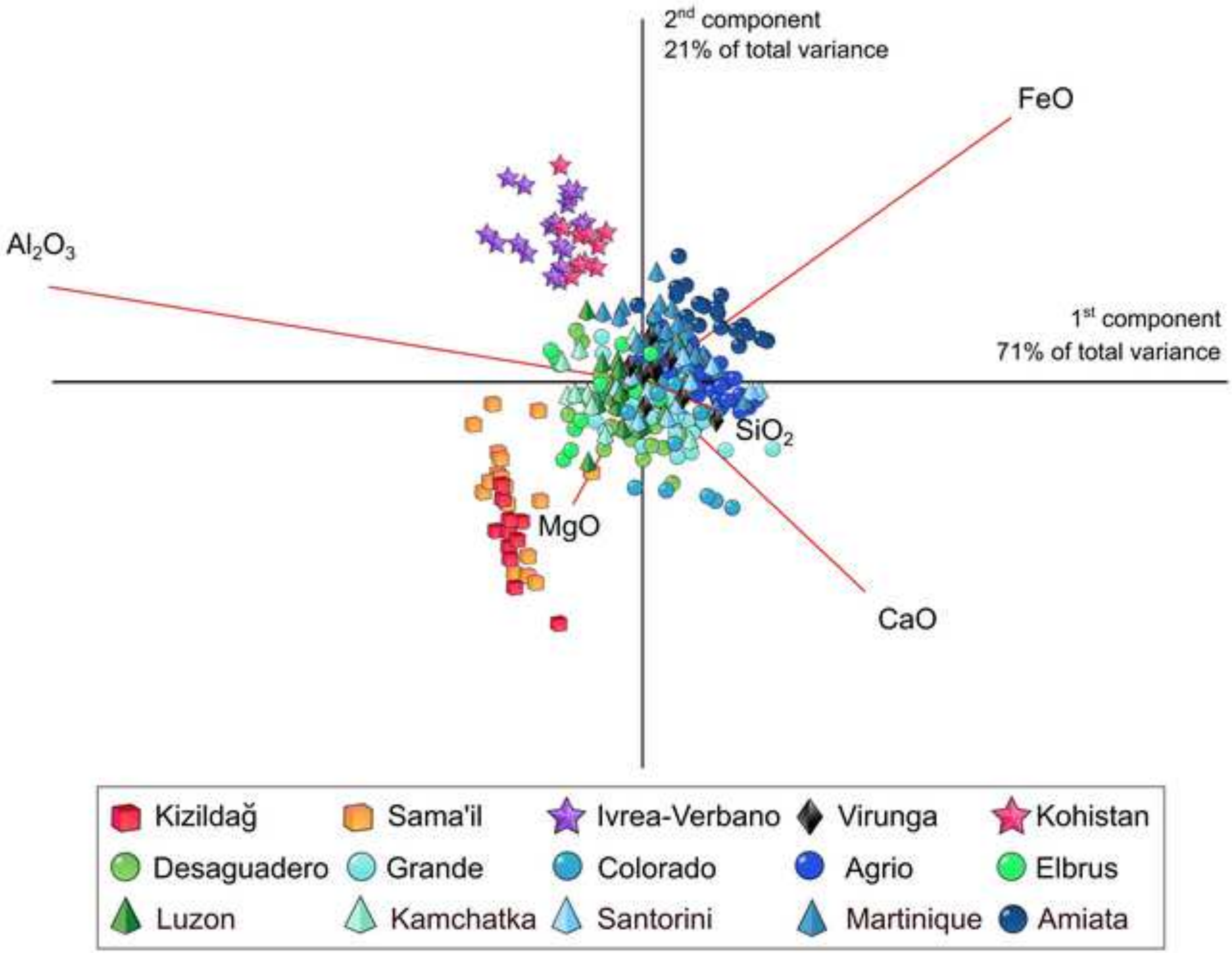

2nd component
21% of total variance
FeO
Al_2O_3
1st component
71% of total variance
SiO_2
MgO
CaO
Kizildağ
Sama'il
Ivrea-Verbano
Virunga
Kohistan
Desaguadero
Grande
Colorado
Agrio
Elbrus
Luzon
Kamchatka
Santorini
Martinique
Amiata

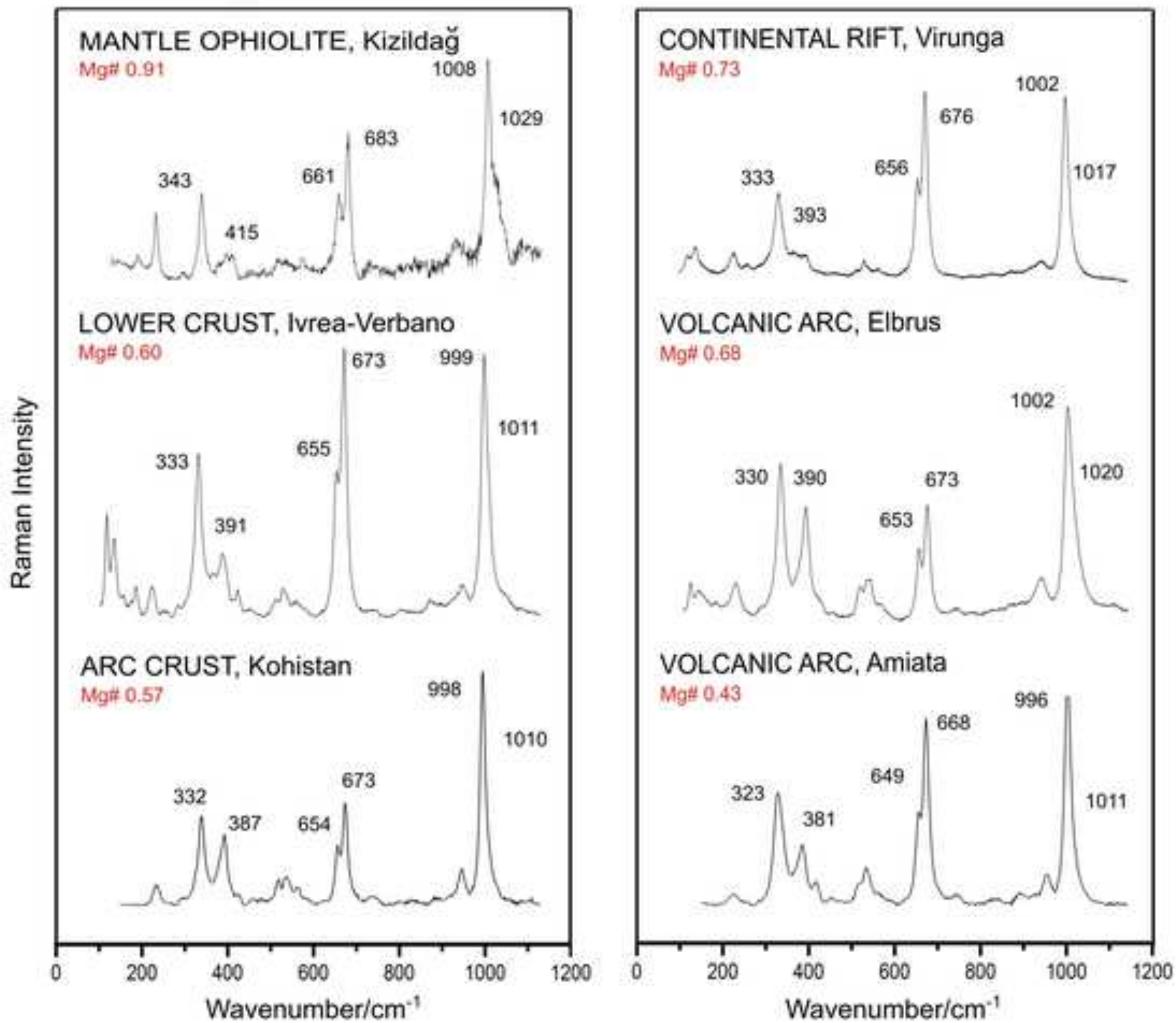
MANTLE OPHIOLITE, Kizildağ
Mg# 0.91
343
415
661
683
1008
1029
LOWER CRUST, Ivrea-Verbano
Mg# 0.60
333
391
655
673
999
1011
ARC CRUST, Kohistan
Mg# 0.57
332
387
654
673
998
1010
CONTINENTAL RIFT, Virunga
Mg# 0.73
333
393
656
676
1002
1017
VOLCANIC ARC, Elbrus
Mg# 0.68
330
390
653
673
1002
1020
VOLCANIC ARC, Amiata
Mg# 0.43
323
381
649
668
996
1011
Raman Intensity
0
200
400
600
800
1000
1200
Wavenumber/cm-1

Figure Click here to access/download;Figure;Figure 6 Borromeo.jpg

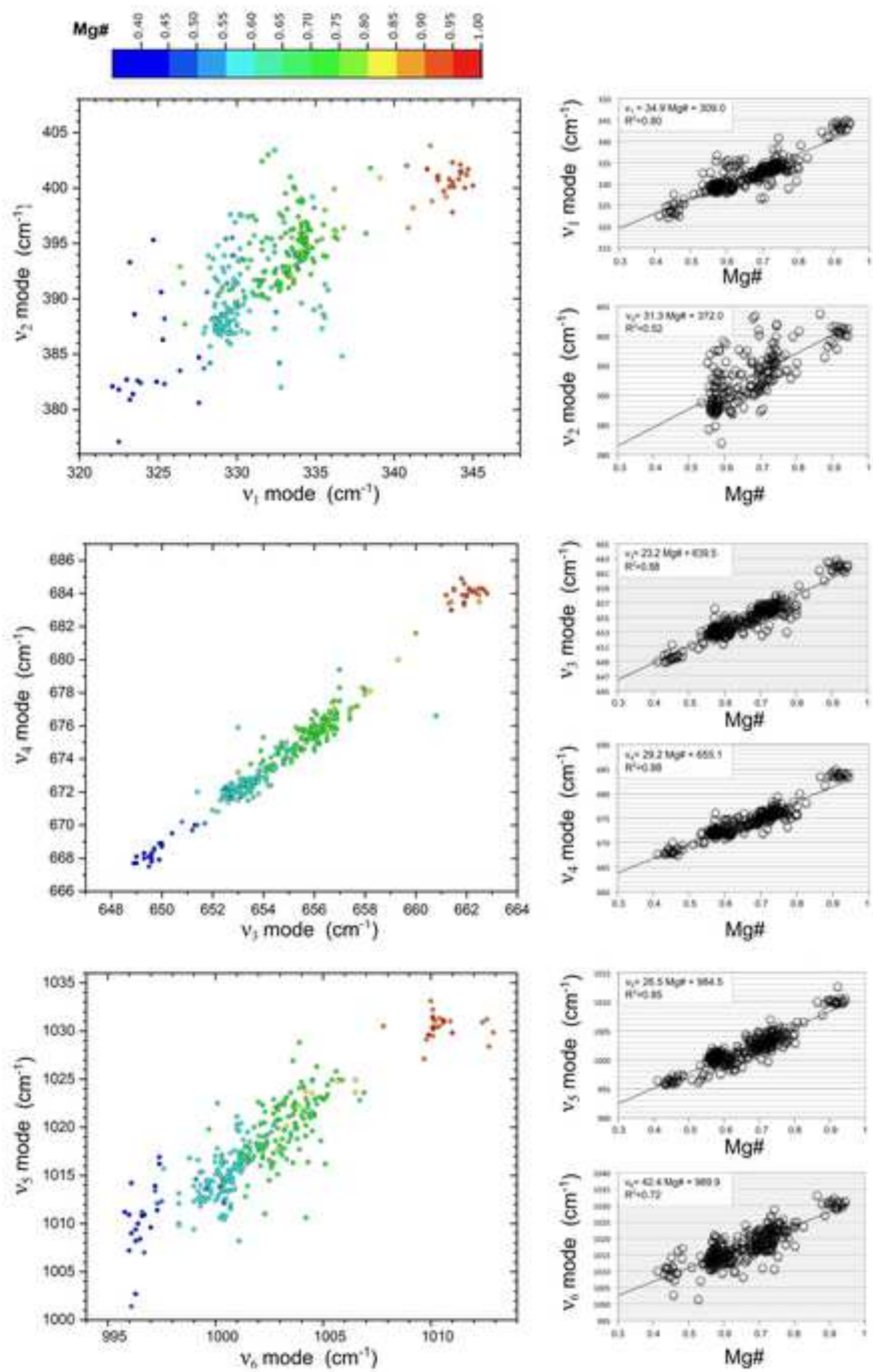

Figure

Click here to access/download;Figure;Figure 7 Borromeo.jpg

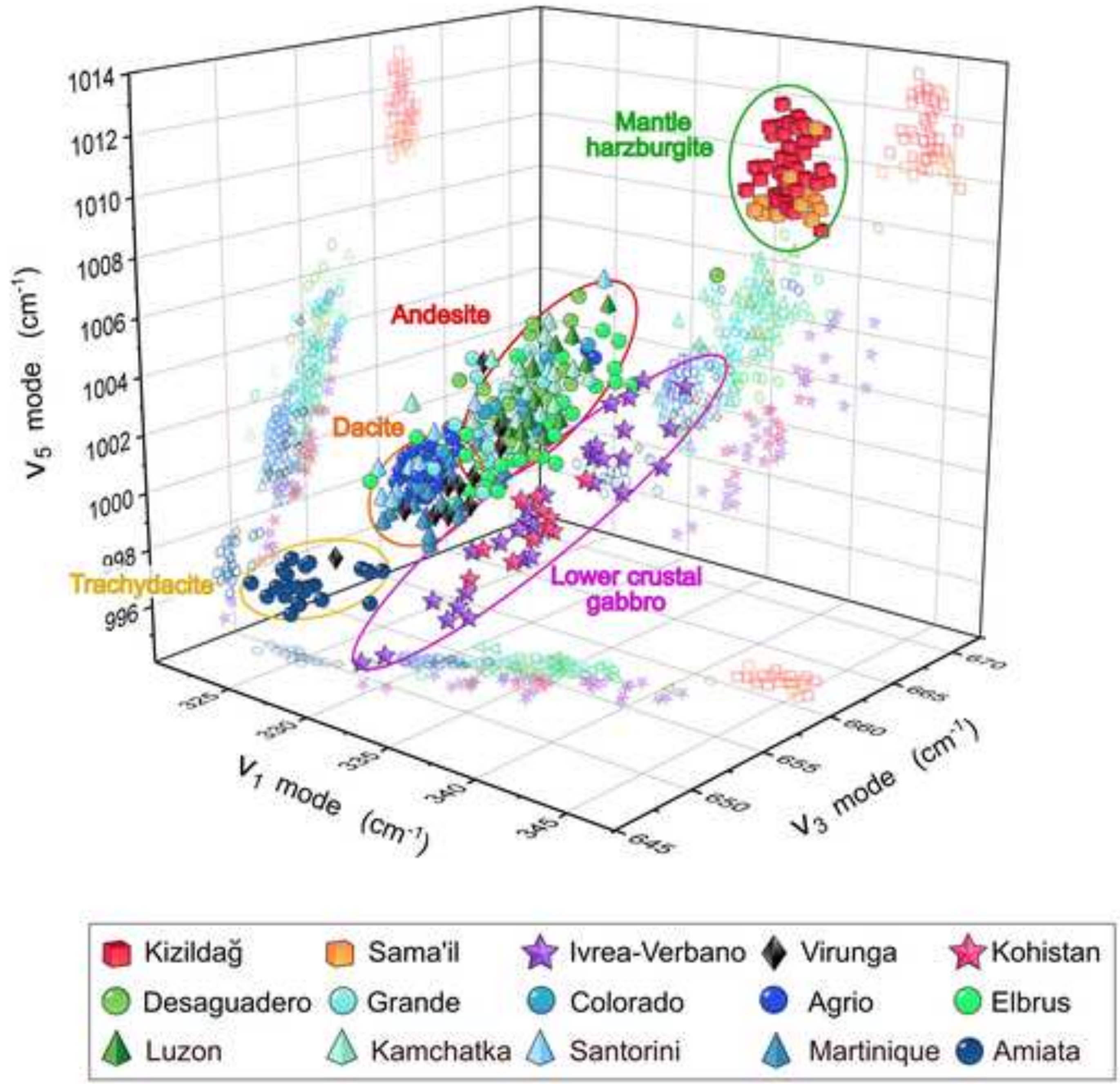

Table

Click here to access/download;Table;Tables Borromeo.xlsx

Structural level	Geodynamic setting	Geological domain	Main lithology	Location
MANTLE	OPHIOLITIC MANTLE	Hatay-Kiziildağ Complex	Harzburgite	Hatay Peninsula (Turkey)
		Sema'il Complex	Harzburgite	Northern Oman Mountains
LOWER CRUST	CONTINENTAL & ARC CRUST	Ivrea-Verbano Mafic Complex	Granulitic gabbro	Southern Alps (Italy)
		Kohistan Arc	Metagabbro to granite	Northern Pakistan
UPPER CRUST	CONTINENTAL MAGMATIC ARC	Andean Cordillera	Andesite and dacite	Río Desaguadero (Argentina)
		Andean Cordillera	Basalt to dacite	Río Grande (Argentina)
		Andean Cordillera	Basalt to dacite	Río Colorado (Argentina)
		Andean Cordillera	Dacite	Río Agrio (Argentina)
	VOLCANIC ARC	Luzon island arc	Basalt to dacite	Taiwan Island
		Kamchatka island arc	Andesite	SE Kamchatcka (Russia)
		Lesser Antilles island arc	Andesite and dacite	Martinique Island
		South Aegean island arc	Andesite and dacite	Santorini Island (Greece)
		Mt. Amiata (Tuscan province)	Trachydacite	Orcia River (Italy)
		Elbrus Volcano	Andesite and dacite	Greater Caucasus (Russia)
	RIFT VALLEY	Virunga volcanic province	K-trachyte and latite	East African Rift (Rwanda)

Geodynamic setting	Unit		SiO_2 wt%	TiO_2 wt%	Al_2O_3 wt%	FeO wt%	MnO wt%	MgO wt%	CaO wt%	K_2O wt%	Na_2O wt%	Cr_2O_3 wt%	Mg#	En mol%	Fe mol%	Wo mol%
OPHIOLITIC MANTLE	Kiziildağ	Mean	56.6	b.d.l.	2.0	5.6	0.02	33.8	1.5	b.d.l.	b.d.l.	0.8	0.92	88.9	8.3	2.9
		Max	57.3	b.d.l.	2.5	5.9	0.2	34.5	2.3	b.d.l.	b.d.l.	1.0	0.96	89.9	8.7	4.2
		Min	56.0	b.d.l.	1.6	5.2	b.d.l.	33.2	0.9	b.d.l.	b.d.l.	0.6	0.91	88.1	7.7	1.6
	Sema'il	Mean	55.4	0.3	2.2	6.8	0.3	32.2	1.2	0.1	0.3	1.1	0.91	87.0	10.7	2.3
		Max	56.6	0.4	3.3	8.8	0.4	33.3	2.1	0.3	0.4	1.4	0.94	88.4	13.9	4.1
		Min	54.3	0.2	0.8	5.8	0.2	31.6	0.6	b.d.l.	0.08	0.7	0.87	84.9	9.3	1.1
CONTINENTAL & ARC CRUST	Ivrea-Verbano	Mean	52.6	0.02	2.4	21.4	0.6	22.2	0.5	b.d.l.	0.02	b.d.l.	0.65	63.4	35.5	1.1
		Max	54.9	0.2	3.6	27.4	0.8	26.5	0.8	b.d.l.	0.2	b.d.l.	0.75	72.9	46.4	1.7
		Min	51.3	b.d.l.	1.6	16.3	0.4	17.6	0.4	b.d.l.	b.d.l.	b.d.l.	0.53	51.9	26.1	0.9
	Kohistan	Mean	51.5	b.d.l.	1.7	24.3	0.5	20.4	0.8	b.d.l.	b.d.l.	b.d.l.	0.61	58.5	40.0	1.6
		Max	52.7	b.d.l.	2.2	25.9	0.8	21.4	1.1	b.d.l.	b.d.l.	b.d.l.	0.63	60.7	43.3	2.4
		Min	50.9	b.d.l.	1.0	23.1	0.3	18.7	0.4	b.d.l.	b.d.l.	b.d.l.	0.57	54.3	37.6	0.7
CONTINENTAL MAGMATIC ARC	Río Desaguadero (Argentina)	Mean	53.9	0.6	1.2	18.0	0.3	24.5	1.6	0.2	0.3	0.02	0.73	68.3	28.5	3.2
		Max	56.2	0.8	2.7	21.1	0.5	30.8	2.0	0.4	0.5	0.5	0.88	82.9	33.7	4.2
		Min	52.3	0.3	0.5	9.7	0.1	22.2	1.0	0.06	0.1	b.d.l.	0.66	63.5	14.8	2.0
	Río Grande (Argentina)	Mean	54.7	0.5	0.9	17.1	0.4	23.2	1.5	0.2	0.4	b.d.l.	0.69	66.7	30.2	3.1
		Max	55.8	0.7	1.6	21.4	0.6	25.5	1.9	0.3	0.8	b.d.l.	0.74	71.7	35.4	3.9
		Min	53.5	0.3	0.2	15.7	0.2	21.1	1.0	0.1	0.2	b.d.l.	0.64	61.3	25.2	2.2
	Río Colorado (Argentina)	Mean	53.9	0.2	0.7	18.6	0.9	24.1	1.6	b.d.l.	0.3	0.02	0.71	66.7	30.3	3.1
		Max	55.1	0.4	1.3	22.0	1.7	26.3	2.4	b.d.l.	0.6	0.3	0.80	71.3	35.6	4.8
		Min	53.1	0.1	0.5	15.4	0.5	21.5	1.1	b.d.l.	0.2	b.d.l.	0.65	61.4	24.3	2.2
	Río Agrio (Argentina)	Mean	53.0	0.4	0.7	24.8	0.6	18.8	1.5	b.d.l.	0.3	b.d.l.	0.58	55.1	41.7	3.2
		Max	54.9	0.7	2.4	27.0	1.1	24.8	2.0	b.d.l.	0.8	b.d.l.	0.74	71.2	44.2	4.2
		Min	50.7	0.2	0.3	15.3	0.3	17.5	1.3	b.d.l.	0.05	b.d.l.	0.55	52.9	25.1	2.5
VOLCANIC ARC	Taiwan	Mean	53.2	0.4	1.2	18.2	0.5	24.8	1.5	0.1	0.2	0.3	0.73	68.2	28.9	2.9
		Max	54.2	0.5	1.7	20.1	0.7	27.5	2.0	0.2	0.4	0.5	0.83	74.9	31.7	3.8
		Min	52.0	0.2	0.7	13.4	b.d.l.	23.6	0.8	b.d.l.	0.09	b.d.l.	0.70	65.4	21.2	1.6
	Kamchatka	Mean	52.5	0.4	1.4	17.9	0.4	25.0	1.6	0.2	0.2	0.09	0.75	68.7	28.2	3.1
		Max	53.5	0.6	2.4	21.1	0.7	26.3	2.0	0.3	0.4	0.2	0.80	71.7	34.2	4.0
		Min	51.5	0.3	0.6	15.9	0.2	22.7	1.0	0.04	0.1	b.d.l.	0.68	63.5	24.6	2.1
	Martinique	Mean	50.5	0.4	0.9	26.1	1.2	19.4	1.4	b.d.l.	0.2	0.3	0.61	54.2	43.0	2.8
		Max	53.4	0.7	1.8	29.4	1.5	21.9	1.6	b.d.l.	0.4	0.5	0.69	59.3	48.1	3.2
		Min	48.4	0.2	0.3	23.5	0.8	17.3	0.9	b.d.l.	b.d.l.	0.1	0.53	49.2	37.7	1.7
	Santorini	Mean	51.0	0.4	0.8	22.7	0.9	22.4	1.6	0.1	0.2	0.01	0.66	59.9	36.9	3.2
		Max	53.6	0.6	1.3	26.7	1.4	43.5	2.2	0.2	0.3	0.07	0.72	66.4	44.9	4.4
		Min	50.7	0.3	b.d.l.	16.1	0.3	18.2	0.4	0.05	b.d.l.	b.d.l.	0.58	52.1	19.2	0.5
	Amiata	Mean	49.8	0.4	0.6	32.0	0.4	14.7	1.5	0.2	0.1	b.d.l.	0.47	43.3	53.6	3.1
		Max	51.5	0.7	1.4	35.0	0.7	17.0	1.8	0.4	0.4	b.d.l.	0.54	49.3	57.9	3.7
		Min	48.5	b.d.l.	b.d.l.	28.6	0.2	13.2	1.1	b.d.l.	b.d.l.	b.d.l.	0.41	38.9	47.3	2.4
	Elbrus	Mean	54.2	0.4	1.3	17.2	0.5	25.7	1.3	b.d.l.	b.d.l.	0.2	0.73	70.2	27.3	2.5
		Max	55.1	0.4	2.6	21.7	0.8	29.0	1.6	b.d.l.	b.d.l.	0.5	0.81	77.7	34.9	3.1
		Min	52.8	0.2	0.5	12.5	0.3	22.9	1.0	b.d.l.	b.d.l.	b.d.l.	0.65	63.3	19.2	1.9
RIFT VALLEY	Virunga	Mean	52.1	0.5	0.9	22.3	0.2	20.9	1.6	b.d.l.	0.2	0.2	0.63	60.2	36.4	3.4
		Max	52.9	0.5	1.1	25.6	0.3	22.8	1.8	b.d.l.	0.3	0.3	0.69	64.8	42.1	3.6
		Min	51.4	0.4	0.5	19.7	0.2	18.7	1.5	b.d.l.	0.2	b.d.l.	0.57	54.6	31.8	3.2

Geodynamic setting	Unit	Mg#		v_1 cm^{-1}	v_2 cm^{-1}	v_3 cm^{-1}	v_4 cm^{-1}	v_5 cm^{-1}	v_6 cm^{-1}
OPHIOLITIC MANTLE	Kiziildağ	**0.92**	**Mean**	**343.4**	**400.8**	**662.1**	**683.8**	**1011.5**	**1030.1**
		0.96	Max	344.3	402.3	662.7	684.6	1012.9	1031.0
		0.91	*Min*	*342.1*	*398.5*	*661.4*	*683*	*1010.1*	*1028.4*
	Sema'il	**0.91**	**Mean**	**343.5**	**400.5**	**661.9**	**683.9**	**1010.3**	**1030.5**
		0.94	Max	345.0	403.8	662.8	684.9	1012.6	1033.1
		0.87	*Min*	*341.2*	*397.8*	*661.2*	*683.3*	*1009.7*	*1027.1*
CONTINENTAL & ARC CRUST	Ivrea-Verbano	**0.65**	**Mean**	**335.9**	**393.6**	**654.8**	**675.6**	**1000.1**	**1014.6**
		0.75	Max	340.8	402.1	658.0	679.4	1004.2	1022.1
		0.53	*Min*	*332.5*	*384.2*	*652.4*	*672.1*	*996.7*	*1007.0*
	Kohistan	**0.61**	**Mean**	**334.7**	**389.8**	**654.6**	**674.3**	**999.3**	**1013.6**
		0.63	Max	336.7	399.2	656.2	676.0	1001.0	1021.1
		0.57	*Min*	*332.2*	*382.0*	*652.7*	*672.5*	*997.6*	*1009.4*
CONTINENTAL MAGMATIC ARC	Río Desaguadero (Argentina)	**0.73**	**Mean**	**333.7**	**394.4**	**656.1**	**675.8**	**1003.8**	**1021.9**
		0.88	Max	340.9	401.1	660.0	681.6	1007.8	1030.5
		0.66	*Min*	*331.0*	*387.3*	*654.1*	*673.5*	*1001.5*	*1016.8*
	Río Grande (Argentina)	**0.69**	**Mean**	**331.8**	**393.0**	**655.3**	**674.6**	**1002.9**	**1019.9**
		0.74	Max	335.7	397.4	657.4	676.6	1005.2	1024.4
		0.64	*Min*	*326.6*	*387.9*	*652.8*	*672.0*	*1000.3*	*1016.3*
	Río Colorado (Argentina)	**0.71**	**Mean**	**332.9**	**394.5**	**655.9**	**675.3**	**1003.1**	**1018.2**
		0.80	Max	335.1	403.4	657.7	677.2	1005.0	1022.9
		0.65	*Min*	*330.5*	*390.0*	*654.3*	*673.3*	*1001.2*	*1012.8*
	Río Agrio (Argentina)	**0.58**	**Mean**	**329.6**	**390.2**	**653.3**	**672.5**	**1000.9**	**1015.1**
		0.74	Max	336.4	397.6	656.8	677.5	1005.2	1023.4
		0.55	*Min*	*328.4*	*386.8*	*652.6*	*671.6*	*999.8*	*1010.4*
VOLCANIC ARC	Taiwan	**0.73**	**Mean**	**333.8**	**395.0**	**656.4**	**676.2**	**1003.6**	**1019.7**
		0.83	Max	336.2	399.5	658.2	678.1	1006.5	1024.9
		0.70	*Min*	*326.4*	*392.4*	*655.5*	*675.1*	*1002.3*	*1011.0*
	Kamchatka	**0.75**	**Mean**	**333.5**	**393.8**	**656.0**	**675.7**	**1003.6**	**1021.9**
		0.80	Max	336.3	398.0	657.4	677.4	1005.9	1026.3
		0.68	*Min*	*329.0*	*389.3*	*653.0*	*673.2*	*1001.4*	*1016.4*
	Martinique	**0.61**	**Mean**	**329.9**	**390.5**	**653.6**	**672.3**	**1000.0**	**1014.9**
		0.69	Max	332.8	397.4	655.1	674.0	1001.7	1019.8
		0.53	*Min*	*328.0*	*385.7*	*652.0*	*670.9*	*998.3*	*1011.8*
	Santorini	**0.66**	**Mean**	**330.8**	**392.1**	**654.2**	**673.4**	**1001.8**	**1018.4**
		1.00	Max	334.2	402.4	660.8	676.6	1006.7	1022.8
		0.58	*Min*	*327.9*	*386.9*	*651.4*	*670.8*	*999.7*	*1013.8*
	Amiata	**0.47**	**Mean**	**324.9**	**384.8**	**650.0**	**668.7**	**996.6**	**1010.4**
		0.54	Max	328.3	395.3	651.7	670.2	997.5	1016.9
		0.41	*Min*	*322.1*	*377.1*	*648.9*	*667.5*	*995.8*	*1001.4*
	Elbrus	**0.73**	**Mean**	**333.5**	**395.7**	**655.9**	**675.8**	**1002.6**	**1019.5**
		0.81	Max	339.1	400.9	659.3	680.0	1006.5	1024.9
		0.65	*Min*	*326.7*	*387.7*	*652.6*	*671.9*	*999.7*	*1008.2*
RIFT VALLEY	Virunga	**0.63**	**Mean**	**331.1**	**390.8**	**654.1**	**673.1**	**1000.9**	**1016.7**
		0.69	Max	332.5	395.7	655.6	674.6	1004.5	1021.6
		0.57	*Min*	*328.9*	*386.8*	*652.5*	*671.7*	*999.2*	*1012.6*

Vibrational modes	Equations (cm^{-1})	R^2	σMg#
v_1 (~ 330 cm^{-1})	Mg# = ($\mathbf{v_1}$ – 309.0) / 34.9	0.8	0.19
v_2 (~ 395 cm^{-1})	Mg# = ($\mathbf{v_2}$ – 372.0) / 31.3	0.52	0.31
v_3 (~ 655 cm^{-1})	Mg# = ($\mathbf{v_3}$ – 639.5) / 23.2	0.88	0.15
v_4 (~ 675 cm^{-1})	Mg# = ($\mathbf{v_4}$ – 655.1) / 29.2	0.88	0.13
v_5 (~ 1002 cm^{-1})	Mg# = ($\mathbf{v_5}$ – 984.5) / 26.5	0.85	0.16
v_6 (~ 1020 cm^{-1})	Mg# = ($\mathbf{v_6}$ – 989.9) / 42.4	0.72	0.21